INTERNATIONAL JOURNAL FOR NUMERICAL METHODS IN FLUIDS, VOL. 19, 605–639 (1994)

A NEW FULLY COUPLED SOLUTION OF THE NAVIER–STOKES EQUATIONS

G. B. DENG, J. PIQUET,* P. QUEUTEY AND M. VISONNEAU

CFD Group, LMF URA 1217 CNRS, Ecole Centrale de Nantes, 1 Rue de la Noe, F-44072 Nantes Cedex, France

SUMMARY

A fully coupled method for the solution of incompressible Navier–Stokes equations is investigated here. It uses a fully implicit time discretization of momentum equations, the standard linearization of convective terms, a cell-centred colocated grid approach and a block-nanodiagonal structure of the matrix of nodal unknowns. The Method is specific in the interpolation used for the flux reconstruction problem, in the basis iterative method for the fully coupled system and in the acceleration means that control the global efficiency of the procedure. The performance of the method is discussed using lid-driven cavity problems, both for two and three-dimensionai geometries, for steady and unsteady flows.

KEY WORDS Laminar flow Numerical simulation Fully coupled methods Physical Interpolation

1. INTRODUCTION

The main limitations of present Navier–Stokes calculations of three-dimensional incompressible viscous flows lie primarily in the lack of grid resolution of results and subsidiarily in the difficulties associated with turbulence modelling. While the latter problem is not discussed here, the former is often connected to the lack of robustness of the solvers used in that the covergence slows down on fine grids, forbidding a grid-independent rate of convergence.

The difficulty in obtaining a solution of incompressible flow equations results from the lack of a pressure time derivative term in the continuity equation. Several methods have been suggested to overcome this problem and they can be distinguished by the way the incompressibility constraint is enforced. Apart from methods such as the pseudocompressibility method in which the pressure–velocity coupling is simulated with a suitable modification of the continuity equation, the most commonly used methods follow the so-called segregated or *Poisson pressure equation approach*. In this approach the pressure–velocity coupling is solved iteratively, successively updating the velocity variables in the momentum equations and the pressure in a pressure equation, in such a way that solenoidality is satisfied at convergence. The updating procedure is then handled by the well-known 'SIMPLE' or 'SIMPLER' methods[1] or by the 'PISO' method.[2] Efforts to improving the robustness of the pressure solver, which is the key part of the method in that it partly controls its convergence rate, bring significant benefits for the overall procedure.[3] The reason is that the increased stiffness of the three-dimensional pressure matrix

* Author to whom correspondence should be addressed.

CCC 0271–2091/94/190605–35

Received April 1993
Revised April 1994

is the most immediate consequence of an increased grid clustering. However, the main drawback of all these methods, where the pressure–velocity coupling is not enforced at each iteration through the solution of the linearized system, lies in the slowing-down of convergence when the number of grid points increases or when the clustering ratios over curvilinear grids increase.

In the following we only consider the so-called *fully coupled methods* where the momentum equations and the continuity equation are solved simultaneously. The first attempt to solve the momentum equations and the continuity equation in a coupled way was the so-called 'SIVA' algorithm.[4] More recent methods follow the boundary layer practice in which the flow domain is swept from upstream to downstream, implicit differencing of momentum being used for marching stability. Upstream influence through the pressure field has to be accounted for; this is done by introducing some form of forward differencing for the streamwise pressure gradient which allows departure-free behaviour. Such methods have been developed mainly in the framework of the partially parabolic approximation, for instance in Reference 5.

Unfortunately, in References 4 and 5 the coupling between dependent variables is performed only in small subdomains (a cell volume or cells with the same given longitudinal station and girth). In such cases the resulting matrices are easy to handle but poor convergence rates are obtained, especially on fine grids, because of the weak coupling between subdomains. The situation can be improved in some respects with multigrid methods,[6,7] although the fully coupled approach in itself[6] does not appear to bring significant improvements with respect to standard Poisson-based methods.[8,9]

It appears therefore that the coupling between the *solenoidal* velocity field and the pressure has to be performed over the whole domain, in spite of the increased complexity of the algebraic system. Velocity and pressure fields are then simultaneously updated in a linear sense, iterations being performed only to solve for the non-linearity. In contrast with References 6 and 7, where the continuity equation is retained in its primitive form, the present work follows References 10 and 11 in the use of an approximate Poisson equation, but it departs from References 10 and 11 in the choice of coupled dependent variables as well as in the selected iterative method. Other possibilities include the use of a penalty relation as in Reference 12, following a classical practice of finite element techniques. The fully coupled system can be solved by two different methods. The most common is to use direct solvers such as Gaussian elimination[12] or YSMP,[13] which incorporates an efficient LU decomposition, as in References 12 and 14–16. However, direct solvers lead to strong storage limitations which forbid their use in three-dimensional problems. Another possibility is to use *ad hoc* CG-like solvers as in Reference 16 and the present work.

Another important aspect of the present work is the proposal of a new discretization scheme. For most practical flow calculations, first-order upwind or skew upwind schemes are not considered to be accurate enough. Schemes higher than second-order are difficult to apply on a curvilinear co-ordinate system. Thus second-order schemes offer a good compromise. Because centred schemes become unstable when the cell Reynolds number is increased, high-order upwind schemes are often preferred. However, they share the drawback that at least two nodes are involved in the upwind direction. This makes convergence more difficult in recirculation zones. Also, their accuracy becomes questionable on a curvilinear grid system. In the following we propose to use the CPI ('consistent physical interpolation') approach, which ensures second-order accuracy. The resulting scheme has a nine- or 19-point stencil for two- or three-dimensional problems respectively; moreover, it remains stable for high cell Reynolds numbers.

The paper is arranged as follows. The ingredients of the numerical discretization are detailed in Section 2. Since a cell-centred collocated grid approach is used, the most important aspect of the numerics lies in the flux reconstruction problem, which consists of expressing the mass fluxes with respect to nodal unknowns so as to avoid spurious pressure modes (Sections 2.2–2.5).

Other significant aspects include the basis iterative method used for the fully coupled system (Section 3) and conjugate gradient means to accelerate the convergence (Section 3.2). Numerical results (Section 4) concerning the accuracy (Section 4.1) and the efficiency of the method (Section 4.2) provide the information needed to establish constraints for the simulation of a difficult unsteady problem, namely the flow of a viscous fluid in a 3:1:1 three-dimensional cavity, driven by its sliding upper wall, at a Reynolds number of 3200 (Section 5). This example is used to demonstrate that the limitations of the method stem only from physical reasons.

2. THE NUMERICAL APPROACH

2.1. *Master equations*

The governing equations are the unsteady Navier–Stokes equations

$$\nabla \cdot \mathbf{U} = 0, \qquad \frac{\partial \mathbf{U}}{\partial t} + \nabla \cdot \mathbf{U}\mathbf{U} = -\nabla p + \frac{1}{Re} \nabla^2 \mathbf{U}, \tag{1a,b}$$

with the boundary conditions

$$\mathbf{U} = \mathbf{i} \quad \text{for } y = 1, \quad \text{where } \mathbf{i} \text{ is the unit vector along the } x\text{-axis}, \tag{2a}$$

$$\mathbf{U} = \mathbf{0} \quad \text{on other sides or faces of the cavity}, \tag{2b}$$

and the initial condition

$$\mathbf{U}(x, y, z)|_{t=0} = \mathbf{0}. \tag{2c}$$

Equations (1) with boundary and initial conditions (2) are solved in the primitive variable convective formulation on a cell-centred collocated grid. A three-level second-order backward Euler scheme is chosen for time discretization:

$$\nabla \cdot \mathbf{U}^{(n+1)} = 0,$$
$$\frac{3\mathbf{U}^{(n+1)} - 4\mathbf{U}^{(n)} + \mathbf{U}^{(n-1)}}{2\Delta t} + \nabla \cdot (\mathbf{U}^{(n+1,\nu-1)}\mathbf{U}^{(n+1)}) = -\nabla p^{(n+1)} + \frac{1}{Re} \nabla^2 \mathbf{U}^{(n+1)}, \tag{3a,b}$$

where the iterative index ν, for which the solution at actual time t^{n+1} is calculated, is omitted. A second-order time-accurate scheme has been found necessary for the simulation of unsteady problems; however, only a standard first-order time-accurate one-step backward Euler method is used for the solution of the steady equations.

Spatial derivatives are treated implicitly by using a central difference scheme on a cell-centred collocated grid around point $\{x_i, y_j, z_k\}$. They involve velocity and pressure unknowns at points indexed with integer values of i, j, k (Figure 1(a)) which are the centres of the control volumes. However, first-order derivatives of the velocity field in (3) require intermediate values (fluxes) to be defined at faces of the control volume

$$\mathbf{V}_{ijk} = \{x_{i-1/2} \leqslant x \leqslant x_{i+1/2}, y_{j-1/2} \leqslant y \leqslant y_{j+1/2}, z_{k-1/2} \leqslant z \leqslant z_{k+1/2}\}.$$

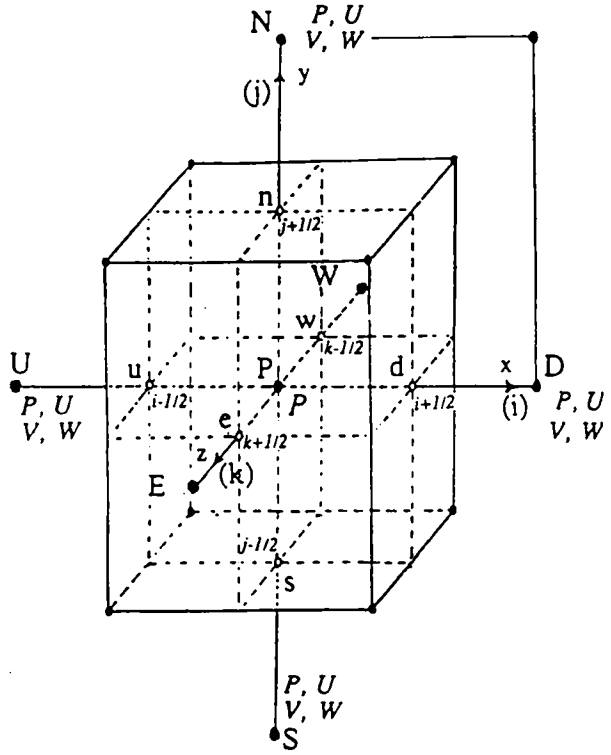

Figure 1(a). Cell-centred three-dimensional collocated grid: ●, locations of unknowns P, U, V, W (U, V, W are Cartesian velocity components, ○, locations where fluxes are required

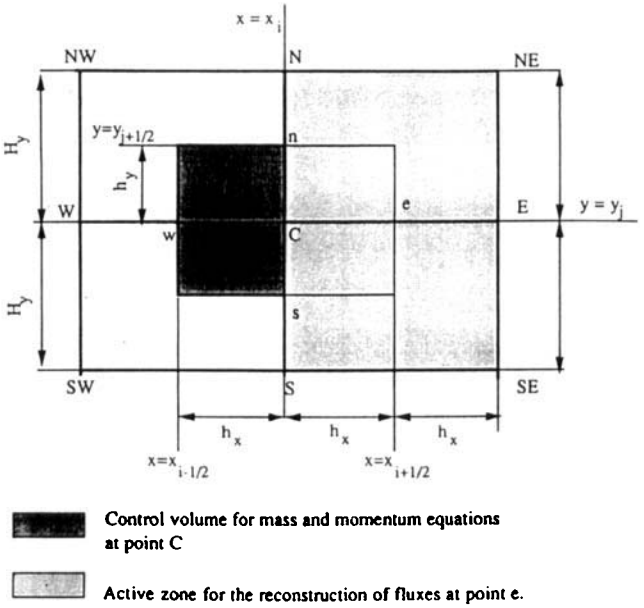

Figure 1(b). Cell-centred two-dimensional collocated grid: influence stencil of point e and notations for the CPI closure

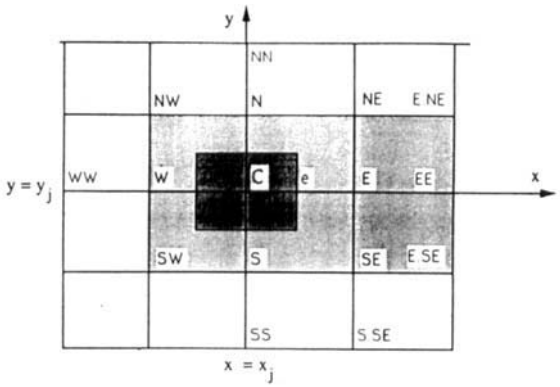

Figure 1(c). Rhie and Chow's influence stencil of point e

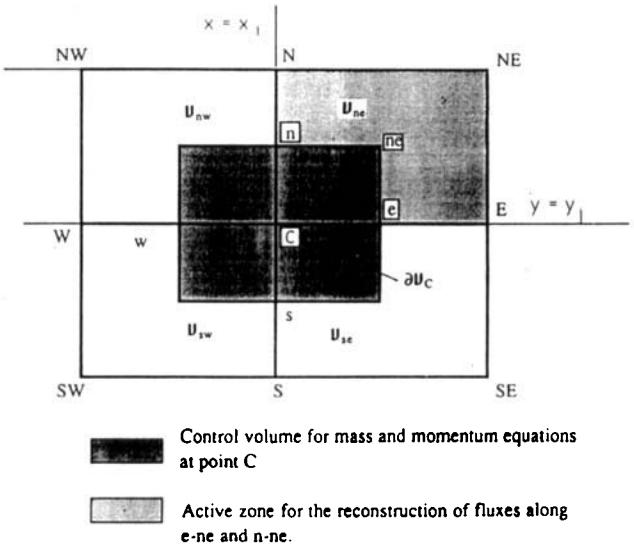

Figure 1(d). Schneider and Raw's influence stencil of point e

Thus on a uniform grid of steps H_x, H_y, H_z, the continuity equation is discretized in the form

$$\frac{U_{i+1/2,j,k} - U_{i-1/2,j,k}}{H_x} + \frac{V_{i,j+1/2,k} - V_{i,j-1/2,k}}{H_y} + \frac{W_{i,j,k+1/2} - W_{i,j,k-1/2}}{H_z} = 0, \qquad (4a)$$

where U, V, W denote the Cartesian components of the velocity vector $\mathbf{U}$.

According to (3b), the momentum equation is discretized with the centred conservative scheme

$$\left.\frac{\partial U}{\partial t}\right|_{i,j,k} + A_x(\mathbf{U})_{i,j,k} + \frac{P_{i+1,j,k} - P_{i-1,j,k}}{2H_x} = \frac{1}{Re}(\nabla^2 U)_{i,j,k},$$
$$\left.\frac{\partial V}{\partial t}\right|_{i,j,k} + A_y(\mathbf{U})_{i,j,k} + \frac{P_{i,j+1,k} - P_{i,j-1,k}}{2H_y} = \frac{1}{Re}(\nabla^2 V)_{i,j,k}, \tag{4b}$$
$$\left.\frac{\partial W}{\partial t}\right|_{i,j,k} + A_z(\mathbf{U})_{i,j,k} + \frac{P_{i,j,k+1} - P_{i,j,k-1}}{2H_z} = \frac{1}{Re}(\nabla^2 W)_{i,j,k},$$

where unsteady, advection and diffusion terms are taken as

$$\left.\frac{\partial \mathbf{U}}{\partial t}\right|_{i,j,k} = \frac{3\mathbf{U} - 4\mathbf{U}^{(n)} + \mathbf{U}^{(n-1)}}{2\Delta t}, \tag{5a}$$

$$\mathbf{A}(\mathbf{U})_{i,j,k} = \frac{U^{n+1,\nu-1}_{i+1/2,j,k}\mathbf{U}_{i+1/2,j,k} - U^{n+1,\nu-1}_{i-1/2,j,k}\mathbf{U}_{i-1/2,j,k}}{H_x}$$
$$+ \frac{V^{n+1,\nu-1}_{i,j+1/2,k}\mathbf{U}_{i,j+1/2,k} - V^{n+1,\nu-1}_{i,j-1/2,k}\mathbf{U}_{i,j-1/2,k}}{H_y}$$
$$+ \frac{W^{n+1,\nu-1}_{i,j,k+1/2}\mathbf{U}_{i,j,k+1/2} - W^{n+1,\nu-1}_{i,j,k-1/2}\mathbf{U}_{i,j,k-1/2}}{H_z}, \tag{5b}$$

$$(\nabla^2\mathbf{U})_{i,j,k} = \frac{\mathbf{U}_{i+1,j,k} + \mathbf{U}_{i-1,j,k} - 2\mathbf{U}_{i,j,k}}{H_x^2} + \frac{\mathbf{U}_{i,j+1,k} + \mathbf{U}_{i,j-1,k} - 2\mathbf{U}_{i,j,k}}{H_y^2}$$
$$+ \frac{\mathbf{U}_{i,j,k+1} + \mathbf{U}_{i,j,k-1} - 2\mathbf{U}_{i,j,k}}{H_z^2}. \tag{5c}$$

The superscript$^{[n+1]}$ corresponding to the actual values of U at time t^{n+1} and for the unknown iteration ν is omitted. A_x, A_y, A_z are the Cartesian components of the advective term A.

The success of the numerical approach depends on the way the numerical fluxes $\mathbf{U}_{i\pm1/2,j,k}$, $\mathbf{V}_{i\pm1/2,j,k}$, $\mathbf{W}_{i,j,k\pm1/2}$ in the continuity equation (4a) and in the momentum equation (4b) are interpolated. How these auxiliary unknowns are expressed with respect to the nodal unknowns (in order to be eliminated) will be considered in Section 2.2 for the two-dimensional case (Figure 1(b)).

2.2. The flux closure problem

The interpolation approach needs to be at least second-order accurate to preserve the accuracy of the second-order centred difference scheme (4). Conventional closure methods are based on Taylor series expansions. An integration point value, say $u_e \equiv U_{i+1/2,j}$, is expressed only in terms of dependent variables of the same family. In other words, u_e is a function of $\{U_{ij}\}$, the set of nodal values for the U-velocity component, but it depends neither on $\{V_{ij}\}$ nor on $\{P_{ij}\}$. Although upwinding interpolation formulae can be used to enhance stability, spurious pressure models exist when collocated grids are used for such interpolation formulae. Such difficulties are circumvented by using a physical interpolation approach in which a velocity integration point value u_e is expressed not only in terms of the set of dependent variables $\{U_{ij}\}$ but also in terms of other physical quantities $\{V_{ij}\}$ and $\{P_{ij}\}$.

Rhie and Chow's approach[11] is the most often used (see e.g. References 17–19). In this approach u_e is interpolated by using the two discretized U-momentum equations at C and at E (Figure 1(c)). For two-dimensional problems (on orthogonal as well as on non-orthogonal grids) it will be seen that the interpolation[11] connects each flux to 12 velocity points, so that the continuity equation involves 20 velocity neighbours of point C where the equations (1) are discretized. The alternative used here is to change the interpolation method in order to minimize the number of nodal points required for the flux closure.

In Schneider and Raw's approach[20] the control volume $\mathbf{V}_C$ surrounding node C is defined as the assembly of four control subvolumes $\mathbf{V}_{ne}$, $\mathbf{V}_{nw}$, $\mathbf{V}_{se}$, $\mathbf{V}_{sw}$ (Figure 1(d)), each of which has two faces which belong to $\partial\mathbf{V}_C$. For instance, the faces of $\mathbf{V}_{ne}$ which belong to $\partial\mathbf{V}_C$ are n–ne and e–ne. The conservative form of the momentum equations is written on each control subvolume. One is left with the evaluation of fluxes over eight subfaces defining $\partial\mathbf{V}_C$ at the reference points located at the middle of each segment, such as n–ne and e–ne, defining $\partial\mathbf{V}_C$. Hence closure is required to eliminate the reference to integration point pressures and for the velocity components. Schneider and Raw write a convective form of the momentum equation from which the integration point values are determined in terms of nodal values of the dependent variables; hence the pressure gradients at points such as nne and ene are obtained from a bilinear interpolation involving nodal pressure values at points C, E, NE, NW. In a similar way the diffusion operator at nne and ene involves the nodal velocity values at the same points. Finally the convection operator (written along the streamline) is discretized using locally skewed upwinding.

Such an approach involves three technical drawbacks. (i) On assembly of the various operator approximations into the momentum closure equation, there will result four equations involving the four integration point variables and the nodal values of the dependent variables. Each of these equations may reference more than one integration point variable and consequently a coupled system of equations involving the integration point variables with respect to the nodal variables. Hence a 4×4 inversion is performed to determine the integration point variables in erms of nodal values only. For the sake of simplicity an explicit formula for integration point values in terms of nodal values would be preferable. (ii) Although the additional cost required to perform the inversion scales linearly with the number of elements, it is evident that this procedure is too complex for a three-dimensional extension to be straightforward. (iii) There is an accuracy problem for the diffusion operator at integration point values, since with only four nodal values and the integration point itself, it cannot be made first-order.

Being inspired by Reference 20, the present approach, while more robust than Rhie and Chow's, corrects the three aforementioned drawbacks in a way which is best explained on the following 2D case. We consider for instance the interpolation of u_e as required by (5). We seek an expression of u_e in terms of the nodal unknowns. With such a stencil the closure of u_e will be more compact than that obtained with Rhie and Chow's method, which involves for u_e, besides, P_C, P_E, U_N, U_{NE}, U_C,U_E, U_S, U_{SE}, the values U_{ENE}, U_{ESE}, U_{EE} (Figure 1(c)). Once unknowns such as u_e are eliminated, the molecule for the mass and momentum equations involves the standard nine points for the pressure (five points only for a Cartesian co-ordinate system) but 21 points for the velocity. It is of course possible to deal with such a large stencil, retaining the pseudovelocity components as primary dependent variables. In two dimensions the algebraic problem then involves a 5×5 block nine-diagonal matrix, with a resulting important storage penalty (see Reference 19 for an analysis of this method in the two- and three-dimensional cases).

In contrast, the mass and momentum molecules resulting from the present method, like Reference 20, involve only the standard nine points for the pressure (five points in the Cartesian case) as well as for the velocity components. The closure for u_e, u_n, u_w, u_s is derived by writing a discretized U-momentum equation at points e, n, w, s respectively. Similarly the closure for

v_e, v_n, v_w, v_s is derived by writing a discrete V-momentum equation at the same corresponding points. The corresponding discrete schemes need not be the same as those written at point C to determine the dependent variables; here we use the convective form of the momentum equation and hence for u at points e, n, w, s:

$$L(U) \equiv \frac{\partial U}{\partial t} + U\frac{\partial U}{\partial x} + V\frac{\partial U}{\partial y} + \frac{\partial P}{\partial x} - \frac{1}{Re}\left(\frac{\partial^2 U}{\partial x^2} + \frac{\partial^2 U}{\partial y^2}\right) = 0. \tag{6}$$

At point e equation (6) is discretized by using a finite difference method on the seven points N, C, S, e, NE, E, SE related to the slightly shaded region in Figure 1(b), where spacings are $H_x = 2h_x$, $H_y = 2h_y$. Central difference schemes are used for the pressure gradient and for the diffusion terms, while convective terms are approximated using a first-order upwind scheme in order to ensure stability. The unsteady term is taken second-order in time using a two-level Euler backward scheme

$$\frac{3u_e - 4u_e^n + u_e^{n-1}}{2\Delta t} + u_e^+\frac{u_e - U_C}{h_x} + u_e^-\frac{U_E - u_e}{h_x} + v_e^+\frac{2u_e - U_S - U_{SE}}{2H_y} + v_e^-\frac{U_{NE} + U_N - 2u_e}{2H_y}$$
$$= -\frac{P_E - P_C}{H_x} + \frac{1}{2Re}\left(\frac{U_{NE} - 2U_E + U_{SE}}{H_y^2} + \frac{U_N - 2U_C + U_S}{H_y^2} + 2\frac{U_E - 2u_e + U_C}{h_x^2}\right), \tag{7a}$$

where convection velocities are known from the previous iteration:

$$u_e^+ = \tfrac{1}{2}(u_e^{n+1,\nu-1} + |u_e^{n+1,\nu-1}|), \qquad u_e^- = \tfrac{1}{2}(u_e^{n+1,\nu-1} - |u_e^{n+1,\nu-1}|), \tag{8a}$$

$$v_e^+ = \tfrac{1}{2}(v_e^{n+1,\nu-1} + |v_e^{n+1,\nu-1}|), \qquad v_e^- = \tfrac{1}{2}(v_e^{n+1,\nu-1} - |v_e^{n+1,\nu-1}|). \tag{8b}$$

Similarly the V-momentum equation fixes v_e according to

$$\frac{3v_e - 4v_e^n + u_e^{n-1}}{2\Delta t} + u_e^+\frac{v_e - V_C}{h_x} + u_e^-\frac{V_E - v_e}{h_x} + v_e^+\frac{2v_e - V_S - V_{SE}}{2H_y} + v_e^-\frac{V_{NE} + V_N - 2v_e}{2H_y}$$
$$= -\frac{P_E + P_{NE} - P_S - P_{SE}}{4H_y} + \frac{1}{2Re}\left(\frac{V_{NE} - 2V_E + V_{SE}}{H_y^2} + \frac{V_N - 2V_C + V_S}{H_y^2} + 2\frac{V_E - 2v_e + V_C}{h_x^2}\right). \tag{7b}$$

The closure interpolation formulae are easily derived from (7). The result specifies u_e linearly with respect to U_{NB} *and* P_{NB} (NB = N, C, S, NE, E, SE). It can be written as

$$u_e = \hat{u}_e + D_e^{-1}\frac{P_E - P_C}{H_x} + g_e^u, \quad \text{with } \hat{u}_e \equiv \sum_{NB} C_{NB}U_{NB}, \tag{9a,b}$$

$$v_e = \hat{v}_e + D_e^{-1}\frac{P_E + P_{NE} - P_S - P_{SE}}{4H_y} + g_e^v, \quad \text{with } \hat{v}_e \equiv \sum_{NB} C_{NB}V_{NB}. \tag{9c,d}$$

In (9a,c) g_e is known from previous time steps. The summation over NB (neighbouring nodes) involves node C plus at most three modes among N, S, E, W, plus at most two nodes among NE, NW, SE, SW. The influence coefficients satisfy also in the steady case

$$\sum_{NB} C_{NB} = 1,$$

indicating that variables $\hat{u}_e$ and $\hat{v}_e$ are interpolations from neighbouring nodal values of U and V respectively. This is verified from the values of the non-vanishing influence coefficients in (9a,c) which are given in Appendix I. In contrast with Reference 20 where 4×4 linear systems are solved for integration point values, the present closures are explicit. Consequently they lead to straightforward extensions to three-dimensional problems (Section 4) as well as to curvilinear grids, as realized also for more practical situations treated for instance in Reference 19.

Although a spatially first-order scheme is used, the closure interpolation for u_e which results from (7) is at least second-order accurate: on a uniform grid with, say, positive components of the advection velocity $\mathbf{U}^+(\mathbf{U}^- = 0)$, the truncation error for (5) is estimated as $D_e^{-1}\Theta(x, y)$, where D_e^{-1} and $\Theta(x, y)$ are both $O(H_x + H_y)$ (see Appendix I). More precisely, for, say, positive convection velocities and a uniform spacing $H_x = H_y = H$ in both directions, assuming that nodal values are known exactly, the interpolation error can be evaluated at point C. We find in the steady case that

$$u_e = u_e(\text{Taylor}) - \frac{ReH^2}{8} L(U) + \frac{ReH^3}{64}(2U + V)L(U) - \frac{ReH^3}{16}\frac{\partial}{\partial x}(LU) + \frac{ReH^3}{64}\left[4\frac{\partial V}{\partial x}\frac{\partial U}{\partial y} + 4\left(\frac{\partial U}{\partial x}\right)^2 + (2U + U)\frac{\partial^2 U}{\partial x^2} + 4V\frac{\partial^2 U}{\partial y^2}\right] + O(h^4). \tag{10}$$

Because $L(U) = 0$ is the momentum equation at point C and

$$u_e(\text{Taylor}) = U + \frac{H}{2}\frac{\partial U}{\partial x} + \frac{H^2}{8}\frac{\partial^2 U}{\partial x^2} + \frac{H^3}{48}\frac{\partial^3 U}{\partial x^3} + O(h^4),$$

the reconstruction is third-order accurate on a uniform grid. This accuracy cannot be offered by the closure of Reference 20 because of its treatment of the diffusion term. Owing to the importance of the consistency of the staggered discrete momentum equations (7), this closure approach is named the 'consistent physical interpolation' (CPI) approach. Equation (7a)indicates that fluxes u_e and u_w respond to different pressure gradients, $(P_E - P_C)/2h_x$ and $(P_C - P_W)/2h_x$ respectively, so that the checker-board oscillations can be avoided.

2.3. *Substitution step: pressure equation*

When u_e, expressed by (9a) and corresponding expressions for u_w, v_n, v_s are substituted into the continuity equation, the result is an equation involving pressure unknowns,

$$\text{Div}\left(\frac{1}{D}\,\textbf{Grad}\,P\right)\Big|_C = \text{Div}\,\hat{\mathbf{V}}|_C + f^P, \tag{11}$$

where Div and **Grad** are the discrete divergence and gradient operators such that for a two-dimensional problem

$$\text{Div}\left(\frac{1}{D}\,\textbf{Grad}\,P\right)\Big|_C \equiv \frac{1}{H_y}\left(\frac{1}{D_n}\frac{P_N - P_C}{H_y} - \frac{1}{D_s}\frac{P_C - P_S}{H_y}\right) + \frac{1}{H_x}\left(\frac{1}{D_e}\frac{P_E - P_C}{H_x} - \frac{1}{D_w}\frac{P_C - P_W}{H_x}\right) + f^P, \tag{12}$$

$$\text{Div}\,\hat{\mathbf{V}}|_C \equiv \frac{\hat{u}_e - \hat{u}_w}{H_x} + \frac{\hat{v}_n - \hat{v}_s}{H_y}, \qquad f^P = \frac{2}{\Delta t}\,\text{Div}\,\mathbf{u}^n|_C - \frac{1}{2\Delta t}\,\text{Div}\,\mathbf{u}^{n-1}|_C. \tag{13}$$

This pressure equation (which does not result from the discrete divergence of the momentum equation) can be used directly as the pressure equation in a decoupled approach to determine the pressure field. The resistivity coefficients D and the 'hat' fluxes have already been defined in Appendix I. Equation (11), together with (12) and (13), takes the alternative form (14), where the 'hat' variables have been eliminated:

$$\sum_{NB} K_{NB}^{pu} U_{NB} + \sum_{NB} K_{NB}^{pv} V_{NB} + \sum_{NB} K_{NB}^{pp} P_{NB} = 0. \tag{14}$$

In (14) the summation over NB involves in general the nine neighbouring nodes NE, N, NW, E, C, W, SE, S, SW. However, in the case of Cartesian co-ordinates the pressure equation involves only the five nodes N, S, E, W, C as indicated by

$$K_{NE}^{pp} = K_{NW}^{pp} = K_{SE}^{pp} = K_{SW}^{pp} = 0. \tag{15}$$

The values of the other 19 influence coefficients K^p are given in Appendix II.

2.4. *Substitution step: momentum equations*

The discretized momentum equations can be obtained in a similar way by substituting (9a) and similar equations into (4b). The result can be first written in conservative forms

$$H_y H_x \frac{3U_C - 4U_C^{(n)} + U_C^{(n-1)}}{2\Delta t} + H_y(u_e^* \hat{u}_e - u_w^* \hat{u}_w) + H_x(v_n^* \hat{u}_n - v_s^* \hat{u}_s) + \sum_{NB} K_{NB}^{up} P_{NB}$$

$$= + \frac{H_y H_x}{Re} \text{Div}(\textbf{Grad } U)|_C - g_C^u, \tag{16a}$$

$$H_y H_x \frac{3V_C - 4V_C^{(n)} + V_C^{(n-1)}}{2\Delta t} + H_y(u_e^* \hat{v}_e - u_w^* \hat{v}_w) + H_x(v_n^* \hat{v}_n - v_s^* \hat{v}_s) + \sum_{NB} K_{NB}^{vp} P_{NB}$$

$$= + \frac{H_y H_x}{Re} \text{Div}(\textbf{Grad } V)|_C - g_C^v, \tag{16b}$$

where the summation over NB is a nine-point (conservative) discrete approximation of the pressure gradient. Rather than solving the present momentum system as a Stokes (Laplacian-driven) system in which only the pressure terms and the viscous terms are treated implicitly, it is possible to eliminate the 'hat' variables using the interpolation formulae (9b,d). The result is

$$\sum_{NB} K_{NB}^{uu} U_{NB} + \sum_{NB} K_{NB}^{up} P_{NB} = f^u, \tag{17a}$$

$$\sum_{NB} K_{NB}^{vv} V_{NB} + \sum_{NB} K_{NB}^{vp} P_{NB} = f^v, \tag{17b}$$

The values of the influence coefficients K_{NB}^{uu}, K_{NB}^{up}, K_{NB}^{vp} as well as those of g_C^u, g_C^v, f^u, f^v are given also in Appendix II. Owing to the chosen linearization, it turns out that $K_{NB}^{vv} = K_{NB}^{uu}$.

2.5. *Discussion*

Compared with the original finite element control volume approach,[20] the present finite volume method improves both the accuracy and the matrix conditioning. As already mentioned

above, the interpolation formulae (9) are third-order accurate on a uniform grid, although convective terms are approximated in (7) by a first-order upwinding scheme. The truncation error of the mass and momentum equations has been evaluated for the steady problem on a grid of uniform spacing H using MAPLE.[21] It has been found that the first differential approximation of the continuity equation at point C is

$$\frac{\partial u}{\partial x}+\frac{\partial v}{\partial y}-\frac{H^2}{8}\left[u\frac{\partial}{\partial x}(u_x+v_y)+v\frac{\partial}{\partial y}(u_x+v_y)-\frac{1}{Re}\left(\frac{\partial^2}{\partial x^2}(u_x+v_y)+\frac{\partial^2}{\partial y^2}(u_x+v_y)\right)\right]+\tau_0 = O(H^3). \tag{18}$$

This indicates that the CPI method is second-order accurate for the mass conservation: the leading term of the truncation error is

$$\tau_0=\frac{H^2}{8}\left(\nabla^2 P-\frac{1}{3}\frac{\partial^2}{\partial x\partial y}(u_y+v_x)\right).$$

The first differential approximation of the *linearized* x-momentum equation $LU=0$ at point C is

$$LU+U\left(\frac{\partial U}{\partial x}+\frac{\partial U}{\partial y}\right)-\frac{ReH^2}{8}\left[\left(\frac{\partial U}{\partial x}+\frac{\partial V}{\partial y}\right)LU+U\frac{\partial}{\partial x}(LU)+V\frac{\partial}{\partial y}(LU)\right]+\tau_1^{(L)}=O(H^3), \tag{19}$$

so that the leading term of the truncation error is

$$\tau_1^{(L)}=\frac{H^2}{8}\left\{Re\left[\frac{\partial U}{\partial x}\left(U\frac{\partial U}{\partial x}+V\frac{\partial U}{\partial y}\right)+\frac{\partial U}{\partial y}\left(U\frac{\partial V}{\partial x}+V\frac{\partial V}{\partial y}\right)\right]+\frac{1}{3}\left[\frac{\partial^3(UV)}{\partial y^3}+\frac{\partial^3 U^2}{\partial x^3}+4\frac{\partial^3 P}{\partial x^3}-\frac{2}{Re}\left(\frac{\partial^4 U}{\partial x^4}+\frac{\partial^4 U}{\partial y^4}\right)\right]\right\}.$$

The first differential approximation of the *non-linear* x-momentum equation $LU=0$ at point C is

$$LU+U\left(\frac{\partial U}{\partial x}+\frac{\partial V}{\partial y}\right)-\frac{ReH^2}{8}\left[\left(2\frac{\partial U}{\partial x}+\frac{\partial V}{\partial y}\right)LU+U\left(U\frac{\partial}{\partial x}(U_x+V_y)+V\frac{\partial}{\partial y}(U_x+V_y)\right)\right]+\tau_1^{(NL)} = O(H^3),$$

so that the leading term of the truncation error at point C is

$$\tau_1^{(NL)}=-\frac{ReH^2}{8}\left(U^2\frac{\partial^2 U}{\partial x^2}+V^2\frac{\partial^2 U}{\partial y^2}+2UV\frac{\partial^2 U}{\partial x\partial y}+U\frac{\partial P_x}{\partial x}+V\frac{\partial P_x}{\partial y}+U\nabla^2 P\right)-\frac{H^2}{12Re}\left(\frac{\partial^4 U}{\partial x^4}+\frac{\partial^4 U}{\partial y^4}\right)+\frac{H^2}{24}\left[3\left(2U\frac{\partial(\nabla^2 U)}{\partial x}+V\frac{\partial(\nabla^2 U)}{\partial y}\right)+3\frac{\partial}{\partial y}(U\nabla^2 V)+\frac{\partial^3(UV)}{\partial y^3}+\frac{\partial^3 U^2}{\partial x^3}+4\frac{\partial^3 P}{\partial x^3}\right].$$

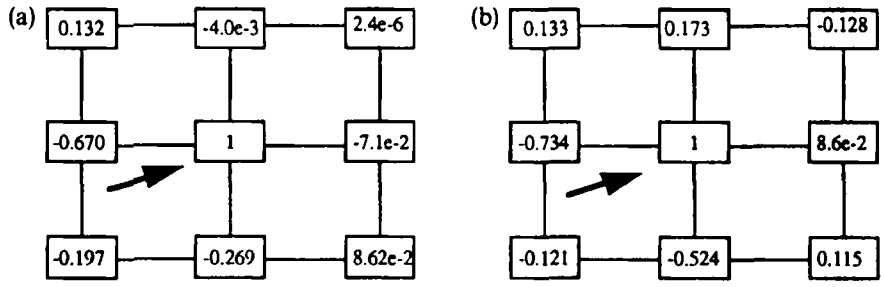

Figure 2. Matrix coefficients for a high-local-Reynolds-number cell with the CPI approach (coefficients are normalized with the central one at point C). (a) Velocity coefficients in the U-momentum equation. (b) Pressure coefficients in the U-momentum equation.

Consequently the CPI scheme for the momentum equation is second-order accurate on a uniform grid. The corresponding expressions for the y-component momentum equation are obtained by a simultaneous permutation of U and V of x and y.

Another important aspect of the CPI approach is related to matrix conditioning. If the grid is orthogonal, it has already been mentioned that the pressure equation (14) involves a five-point stencil for the pressure. Since D is positive, the corresponding pressure matrix is weakly diagonally dominant and is irreducible. Consequently the convergence of conventional iterative relaxation methods is guaranteed for the pressure system (as for Rhie and Chow's method).

Although the CPI scheme builds in an automatic upwinding and hence correct limit behaviours for large and small values of Re, the positivity of the velocity part of the matrix (coefficients K_{NB}^{pu}, K_{NB}^{pv}) is not guaranteed. Hence the CPI scheme may be prone to a cell Reynolds number limitation. This lack of monotonicity remains, however, rather weak and this probably explains the absence of practical difficulties in getting solutions for high values of Re (see Section 4).

Upwinding also applies in the momentum equation both to the convective terms and to the pressure gradient terms through the physical flux interpolation. While such a situation has been analysed in detail on a one-dimensional example,[20,22] its illustration is presented now for the two-dimensional Navier–Stokes equations. Figure 2 indicates significant values of the influence coefficients at a high value of the Reynolds number for a typical nine-point stencil. The arrow indicates the direction of the convection velocity (u_C^*, v_C^*). We can see that both the convection terms and the pressure gradient are significantly upwinded, while the influence coefficients at nodal points around C are not all positive.

2.6. *Pressure boundary conditions*

A cell-centred grid is preferred in the present study since it appears to make the implementation of pressure boundary conditions easier. On a boundary cell the numerical fluxes at inner faces $\mathbf{F}_e$, $\mathbf{F}_n$ and $\mathbf{F}_w$ are determined by the CPI approach in the same way as for any standard point. The numerical flux at the boundary face $\mathbf{F}_s$ is specified directly from the velocity boundary conditions. The resulting pressure equation does not need any additional boundary condition for its resolution in so far as boundary cells are orthogonal at the boundaries. The pressure gradient required for the momentum equations can be calculated in a forward/backward way or by using extrapolated boundary pressure values, which are also used as numerical pressure boundary conditions in the case of a non-orthogonal grid.

3. THE RESOLUTION APPROACH

3.1. The fully coupled approach

Using the previously described method leads to a linearized fully coupled system consisting of equations (17a), (17b) and (14) written at each inner point C(i, j) in the computational space. It has to be solved at each time step t^{n+1} for each iteration v, velocity and pressure fields being updated simultaneously to account for the non-linearity.

We group the three unknowns U, V, P at each grid point (i, j) to define the three-component vector $\mathbf{X}(i, j) \equiv \| U, V, P \|^{\mathrm{T}}$ and we order the unknowns from values $i = 1$ to $i_{\max}$ and for any given value of i from $j = 1$ to $j_{\max}$. When the $i(j-1)$th, ijth and $i(j+1)$th rows of the matrix $\mathbf{A}$ corresponding to (16a), (16b) and (13) are also grouped in this order, the matrix $\mathbf{A}$ appears as a 3×3 block nine-diagonal matrix whose non-vanishing elements in the ijth 3×3 block row located on the $(i-1)(j-1)$th, $(i-1)$th, $(i-1)(j+1)$th columns (influence coefficients of points SW(i, j), W(i, j), NE(i, j) respectively), the $i(j-1)$th, ijth, $i(j+1)$th columns (influence coefficients of points S(i, j), C(i, j), N(i, j) respectively) and the $(i+1)(j-1)$th, $(i-1)j$th, $(i+1)(j+1)$th columns (influence coefficients of points SE(i, j), E(i, j), NE(i, j) respectively). Appendix III presents the resulting matrix $\mathbf{A}$ and the detailed structure of a characteristic elementary block; this demonstrates the optimal compactness of the CPI method with respect to Reference 11. The algebraic fully coupled system $\mathbf{AX} = \mathbf{b}$ is thus written symbolically as

$$\mathbf{A}_{\mathrm{C}}\mathbf{X}_{\mathrm{C}} + \sum_{nb} \mathbf{A}_{nb}\mathbf{X}_{nb} = \mathbf{b}_{\mathrm{C}}. \tag{20}$$

Owing to the collocative character of the approach, the construction of block iterative methods for (20) is made technically easier than if a staggered grid approach were used. With a preconditioning matrix $\mathbf{M}$ and the residual matrix $\mathbf{N}(\mathbf{A} = \mathbf{M} - \mathbf{N})$ the basis iterative method can be written as

$$\mathbf{X}^{(k+1)} = \mathbf{M}^{-1}(\mathbf{b} + \mathbf{N}\mathbf{X}^{(k)}) \tag{21}$$

and its efficiency as a means to solve (20) depends on the choice of $\mathbf{M}$. A block point Jacobi method $\mathbf{M} = \mathrm{diag}(\mathbf{A}) = \| \ldots \mathbf{0} \ldots \mathbf{A}_{\mathrm{C}} \ldots \mathbf{0} \ldots \|$ is a vectorizable preconditioner which only needs the inversion of the 3×3 submatrix coefficients at point C, consisting of the 3×3 block of influence coefficients at point C(i, j). Other blockpoint iterative methods (SOR, Zebra) can be as easily applied. Block line iterative methods retain the 3×3 block tridiagonal matrices $\| \ldots \mathbf{0} \ldots \mathbf{A}_{\mathrm{W}}, \mathbf{A}_{\mathrm{C}}, \mathbf{A}_{\mathrm{E}} \ldots \mathbf{0} \ldots \|$ or $\| \ldots \mathbf{0} \ldots \mathbf{A}_{\mathrm{S}}, \mathbf{A}_{\mathrm{C}}, \mathbf{A}_{\mathrm{N}} \ldots \mathbf{0} \ldots \|$ of discrete points along an x-line (W, C, E) or y-line (S, C, N). $\mathbf{M}$ is then efficiently solved using a block version of the Thomas algorithm. However, such methods in 3D require 81 working matrices in order to store the factorizations and they have been found less efficient than ILU decomposition methods, especially when the grid is stretched in more than one direction.

The block ILU decomposition is such that $\mathbf{M} = \mathbf{L}\mathbf{D}^{-1}\mathbf{U}$, where $\mathbf{D}$ is a 3×3 block diagonal matrix which is determined according to $\mathrm{diag}\ \mathbf{A} = \mathrm{diag}(\mathbf{L}\mathbf{D}^{-1}\mathbf{U})$. The simplest way to construct $\mathbf{L}$ and $\mathbf{U}$ is to take

$$\mathbf{L} = \| \ldots \mathbf{0} \ldots \mathbf{A}_{\mathrm{SW}}, \mathbf{A}_{\mathrm{S}}, \mathbf{0} \ldots \mathbf{0} \ldots \mathbf{A}_{\mathrm{W}}, \mathbf{D}, \mathbf{0} \ldots \mathbf{0} \ldots \|, \tag{22a}$$

$$\mathbf{U} = \| \ldots \mathbf{0} \ldots \mathbf{0}, \mathbf{D}, \mathbf{A}_{\mathrm{E}} \ldots \mathbf{0} \ldots \mathbf{0}, \mathbf{A}_{\mathrm{N}}, \mathbf{A}_{\mathrm{NE}} \ldots \mathbf{0} \ldots \|, \tag{22b}$$

where $\mathbf{A}_{\mathrm{SE}}$ and $\mathbf{A}_{\mathrm{NW}}$ have been put to zero in $\mathbf{L}$ and $\mathbf{U}$ respectively in order to allow the

vectorization to be performed along the diagonal line $x + y = \text{const.}$[19] For lid-driven cavity problems the block diagonal matrix (point Jacobi) is used since it has been found to be the most efficient preconditioner on vector computers. In contrast, block ILU preconditioners should rather be used on curvilinear grids.[19]

3.2. *Conjugate gradient acceleration*

For elliptic problems the convergence rate of classical basis iterative methods such as Jacobi or Gauss–Seidel methods is approximately proportional to N^{-2}, N being the number of unknowns per direction. When applied to the solution of the linearized algebraic system resulting from the discretization of the unsteady or steady incompressible Navier–Stokes equations, the behaviour of a block iterative, fully coupled method is about the same. (For segregated methods the convergence rate is small with respect to N^{-2}.[23]) As a result, the number of iterations increases dramatically with the number of grid points. For this reason, convergence acceleration is needed for both steady and unsteady flow calculations, especially in the three-dimensional case. The conjugate gradient (CG) method has been used because it is independent of grid configuration and does not involve any control parameter. Also, our experience indicates that the computational effort for the CG method is competitive with that of the multigrid method when the number of grid points is not too high (say less than 60 per direction).

For a non-symmetric linear system the conjugate gradient squared (CGS) algorithm[24] (see Appendix IV) is found to be very efficient. However, when applied to a non-linear problem with conventional (non-Newton) linearization, the computational effort is prohibitive. This is because the CGS method does not satisfy a minimization property so that a non-monotonic decrease in the error is found, even for an unsteady simulation where the time step remains small. A variant of CGS, the so-called 'BiCGSTAB' algorithm[25] (Appendix IV), is used since it allows a smoother convergence and a better efficiency for time-dependent problems. The efficiency of a CG method depends on the condition number of the matrix problem. Linearized algebraic equations resulting from the discretization of the Navier–Stokes equations are usually ill-conditioned, especially when large grid aspect ratios are used. Preconditioning is then needed and, as mentioned above, a block diagonal Jacobi preconditioner is used.

3.3. *Defect correction approach*

The convergence of the resulting algebraic system has been found to be slow when the Reynolds number is increased, where flow recirculation exists. Then the flow may have opposite convective directions on some control volumes, as shown in Figure 3(b). With a large cell Reynolds number the diagonal term may lose its dominance. As a result, the condition number of the matrix increases considerably. The resulting three-dimensional linearized system cannot be solved even with a block ILU preconditioner. An alternative defect correction approach is adopted here, since the diagonal dominance of the momentum equations can always be ensured, using a positive scheme to discretize the convective form of the transport equations. The principle of the method is as follows. Let $L_1 U = b$ be the discrete problem to be solved using the previously described CPI method. A defect correction approach is written for the momentum equations as

$$L_2 U^{(n+1)} = L_2 U^{(n)} + b - L_1 U^{(n)}, \quad n = 1, 2, 3, \ldots, \tag{23a}$$

or

$$L_2 \Delta U^{(n+1)} = R^{(n)}, \quad \text{with } U^{(n+1)} = U^{(n)} + \Delta U^{(n+1)}, \; R^{(n)} = g - L_1 U^{(n)}, \tag{23b}$$

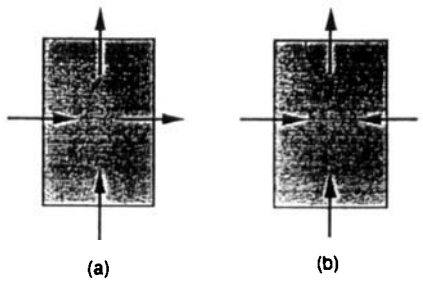

Figure 3. (a) 'Regular' situation. (b) Need for defect correction approach

if L_2 is a linear operator. L_1 is the 'explicit' centred discrete operator (4a,b) applied to (3) which gives global second-order accuracy. L_2 is a linear implicit operator which provides convergence and is based on

$$\nabla \cdot \mathbf{U}^{(n+1)} = 0, \qquad \frac{3\mathbf{U}^{(n+1)} - 4\mathbf{U}^{(n)} + \mathbf{U}^{(n-1)}}{2\Delta t} + (\mathbf{U}^{(n)} \cdot \nabla)\mathbf{U}^{(n+1)} = -\nabla p^{(n+1)} + \frac{1}{Re}\nabla^2 \mathbf{U}^{(n+1)}, \tag{24}$$

where the convective transport equations are discretized using the multiexponential scheme[13] (or any other upwind-like positive scheme). Also, since the discretization resulting from the CPI approach is retained in (24) for the continuity equation, as in the explicit operator, the mass conservation is ensured when the solution is updated. No convergence problem has been found so far with this defect correction approach.

4. RESULTS

4.1. Accuracy of the CPI method

The classical 2D square driven cavity problem $0 \leqslant x \leqslant 1$, $0 \leqslant y \leqslant 1$ with $U(x, 1) = 1$ is used to qualify the accuracy of the CPI approach (Figure 4, right). Tables I and II compare with reference results[26] significant values of minimal and maximal centreline velocities at $Re = 400$ and 1000 respectively. Calculations have been performed on three different uniform grids from which the error has been estimated as well as the presumed order of accuracy of the present CPI method. The determination of the presumed order of accuracy is based on the argument given in Appendix V. Residuals are reduced by more than six orders of magnitude in order to get a fully converged solution. The estimated 'exact values' and order of accuracy are given in the tables; they confirm the second order of accuracy of the method established by formulae (18) and (19).

The accuracy of the present approach compares favourably not only with that of upwind-type schemes such as finite analytic,[27] uniexponential[13] and multiexponential[13] schemes but also with that of a centred scheme, either written on a staggered grid (so as to avoid flux interpolation) or using Rhie and Chow's interpolation. This last case was found to converge only for $Re = 400$.

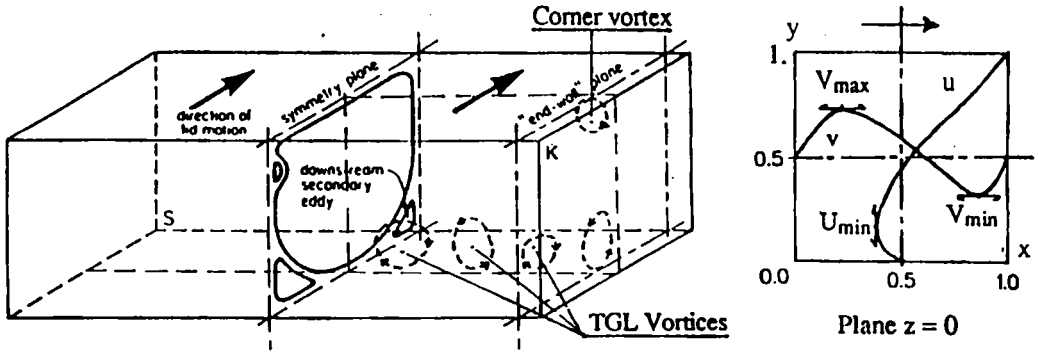

Figure 4. Definitions for lid-driven cavity flows

For $Re = 1000$ the non-linear iteration procedure diverged, although linear systems were correctly solved. Moreover, the improvement with respect to staggered grid results increases with the Reynolds number. This demonstrates, if necessary, the controlling influence of the flux closure on the global accuracy of the scheme.

The cubic lid-driven cavity flow where the driving face is $y = 1$ is now considered because it provides an interesting benchmark test case for three-dimensional methods. In contrast with its two-dimensional counterpart which is the most often used test case, only a limited number of steady flow calculations have been performed in the past on the (cubic) 1:1:1 case, usually for low Reynolds numbers (< 1000) and a low grid resolution, with finite difference methods,[28–39] finite elements methods[40] or spectral methods.[41] For Reynolds numbers higher than 1000 the physics of this simple geometry is complex and very few numerical solutions are available:[33,40,42,43] the flow behaviour exhibits significant transverse motions, Taylor–Görtler-like (TGL) vortices, end wall vortices and, for a given Reynolds number, stronger unsteady effects

Table I. Square driven cavity; $Re = 400$

Method	Grid	U_{min}	V_{min}	V_{max}
'CPI' approach	32 × 32	−0·306	−0·428	0·283
'CPI' approach	64 × 64	−0·32368	−0·44862	0·29925
'CPI' approach	96 × 96	−0·32653	−0·45163	0·30183
'CPI' approach	128 × 128	−0·32751	−0·45274	0·30271
Estimated 'CPI' exact		−0·32873	−0·45431	0·30379
Estimated order of accuracy of CPI		2·05	1·85	2·07
Ghia *et al.*[26]	129 × 129	−0·3273	−0·4499	0·3020
Centred Rhie and Chow	128 × 128	−0·32603	−0·45095	0·30119
'CPI' approach	49 × 49	−0·31858	−0·44245	0·29447
Centred scheme (staggered grid)	49 × 49	−0·310	−0·429	0·285
Finite analytic[27]	49 × 49	−0·2960	−0·4051	0·2662
Upwind scheme	49 × 49	−0·2240	−0·3462	0·2101
Multiexponential scheme[13]	49 × 49	−0·2771	−0·3842	0·247
Uniexponential scheme[13]	49 × 49	−0·294	−0·406	0·264

Table II. Square driven cavity; $Re = 1000$

Method	Grid	U_{min}	V_{min}	V_{max}
Ghia *et al.*[26]	129 × 129	−0·3829	−0·5155	0·3709
Bruneau and Jouron[7]	256 × 256	−0·3764	−0·5208	0·3665
'CPI' approach	64 × 64	−0·37436	−0·51015	0·36364
'CPI' approach	96 × 96	−0·38233	−0·51947	0·37109
'CPI' approach	128 × 128	−0·38511	−0·52280	0·37369
Estimated 'CPI' exact		−0·38867	−0·52724	0·37702
Estimated order of accuracy		2·01	1·94	2·01
Centred scheme (staggered grid)	64 × 64	−0·35726	−0·48858	0·34556
Centred scheme (staggered grid)	96 × 96	−0·37441	−0·50982	0·36271
Centred scheme (staggered grid)	128 × 128	−0·38050	−0·51727	0·36884
Estimated centred exact		−0·38855	−0·52690	0·37705
Estimated order of accuracy		1·96	1·94	1·99
Finite analytic[27]	129 × 129	−0·3689	−0·5037	0·3553
Multiexponential scheme[13]	129 × 129	−0·3460	−0·4858	0·3330

than in the 2D case. This situation is unfortunate, since significant numerical experiments cannot be realized for the three-dimensional case, while Hopf bifurcation, periodicity, period doubling and numerical transition to chaos have been observed numerically only in two dimensions, owing to the lack of computer resources.

Figure 5 shows for $Re = 100$, 400 and 1000 the steady velocity profiles obtained in the symmetry plane, on the appropriate centrelines, with a 64 × 64 × 32 grid resolution of the (half) cubic cavity (32 points along z, with a symmetry condition imposed on the plane $z = 0·5$). Significant three-dimensional results on a 64 × 64 grid concerning the flow in the z-symmetry plane are presented in Table III.

To make evident the global differences from the two-dimensional case, the velocity profiles in the symmetry plane $z = 0·5$ are compared with their two-dimensional counterparts in a steady case for three different Reynolds numbers, namely $Re = 400$ (Figure 5(a)), $Re = 400$ (Figure 5(b)), $Re = 1000$ (Figure 5(c)). U-velocity profiles are presented along the centreline ($x = 0·5$, $z = 0·5$) and V-velocity profiles are presented along the centreline ($y = 0·5$, $z = 0·5$). They appear less steep in the 3D case than in the 2D case because of the global divergence of the flow away from the symmetry plane. Symbols '○' indicate the two-dimensional results of Ghia *et al.*[26] while 2D and 3D pseudospectral results[41] are indicated by symbols '+' and '△' respectively. Grid dependence is studied for the case $Re = 400$, where two grids have been used: 32 × 32 × 16 (- - - -) and 64 × 64 × 32 (——). Compared with the results of Reference 41, discrepancies are observed mainly on the V profile near the downstream wall, even with the finest grid. This is due to the use in Reference 41 of a regularized velocity profile U along the edges of the plane $y = 1$ in order to avoid discontinuous boundary conditions which would destabilize spectral-type calculations. Such results also indicate that the grid resolution in the x and y-directions needs to be nearly the same in 2D and 3D problems. According to the error estimation used for the two-dimensional problem, the relative error $(U - U_{exact})/U_{exact}$ for the CPI method on the 64 × 64 × 32 grid is about −0·4%, −1·5% and −4% for $Re = 100$, 400 and 1000 respectively. The appropriate grid resolution for the 3D case is thus 'extrapolated' from the 2D case: with a 64 × 64 uniform grid good results are obtained for $Re = 1000$ (Figure 5(c)) and reasonable

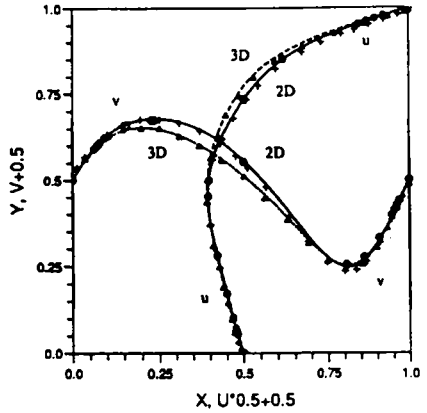

Figure 5(a). Cubic driven cavity, $Re = 100$, grid 64 × 64 × 32. Velocity profiles on vertical and horizontal centrelines in z-symmetry plane: ○, 2D results;[26] +, 2D results;[41] +, 3D results;[41] ——, present 2D 'CPI' results; broken lines, present 3D 'CPI' results

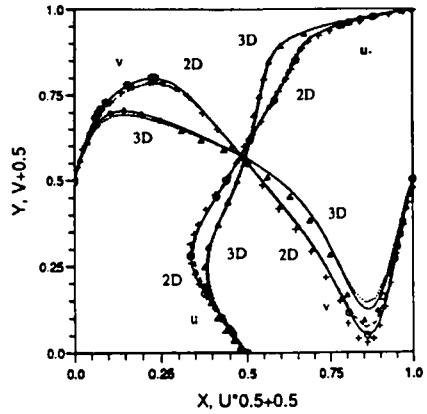

Figure 5(b). Cubic driven cavity, $Re = 400$, grid 64 × 64 × 32. Velocity profiles on vertical and horizontal centrelines in z-symmetry plane: ○, 2D results;[26] +, 2D results;[41] △, 3D results;[41] ——, present 2D and 3D 'CPI' results, grid 64 × 64 × 32; -·-·-, present 2D 'CPI' results for V, grid 32 × 32; ·····, present 3D 'CPI' results for V, grid 32 × 32 × 16; – – –, present 2D 'CPI' results for U, grid 32 × 32; ----, present 3D 'CPI' results for U grid 32 × 32 × 16

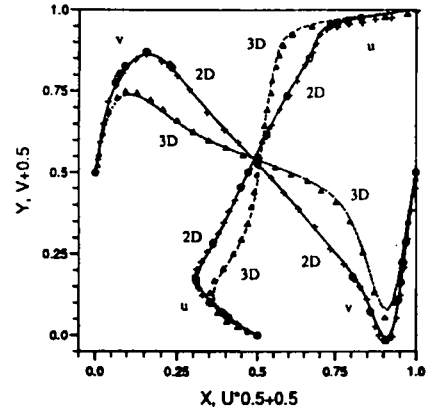

Figure 5(c). Cubic driven cavity, $Re = 1000$, grid 64 × 64 × 32. Velocity profiles on vertical and horizontal centrelines in z-symmetry plane: ○, 2D results;[26] +, 2D results;[41] △, 3D results;[41] ——, present 2D 'CPI' results; broken lines, present 3D 'CPI' results

Table III

Re	U_{min}	V_{min}	V_{max}
100	−0·21488	−0·24846	0·15228
400	−0·23302	−0·37647	0·20456
1000	−0·27152	−0·42251	0·23912

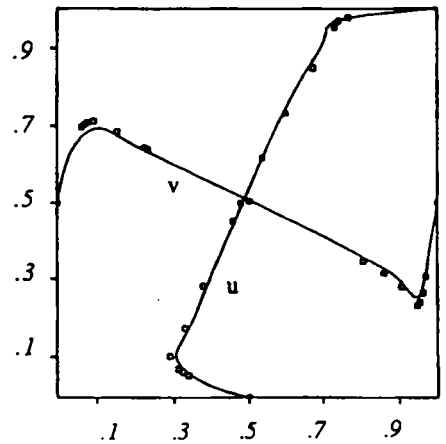

Figure 6. Square driven cavity, $Re = 3200$. Velocity profiles on vertical and horizontal centrelines: □, 2D results;[26] ——, present 'CPI' results, grid 65 × 65

results are found for $Re = 3200$ (Figure 6). This information is used to establish the grid resolution in Section 5.

4.2. *Efficiency of the fully coupled method for a steady flow calculation*

The efficiency of accelerated fully coupled methods can be discussed from Figure 7, obtained for the 2D square driven cavity at $Re = 400$. The evolution with grid refinement of the computational effort σ (CPU time per grid point on VP200) is considered in two cases for which a residual reduction of six orders of magnitude is achieved. The increase in σ with the number of points N per direction is quicker than N^2 for the segregated (PISO-like) method[13] in which the pressure solver is a ILU-PBCG method (although the curve is not drawn for high values of N, since this level of convergence is no longer obtained in a reasonable CPU time on a fine grid). In contrast, the present fully coupled method gives an asymptotic behaviour $\sigma = O(N)$, also with CG acceleration (CGS method). Present slight departures from the linear trend are believed to be due to the defect correction approach and to the CG-like solver. For three-dimensional problems the computational effort remains similar: for steady flow calculations on a 64 × 64 × 32 grid at $Re = 100$ and 400 a residual reduction of four orders of magnitude requires 5.3 and 6.7 ms/point on a VP200 respectively. Having established the efficiency of the method for steady flow calculations, the investigation of its properties for an unsteady flow problem still has to be done.

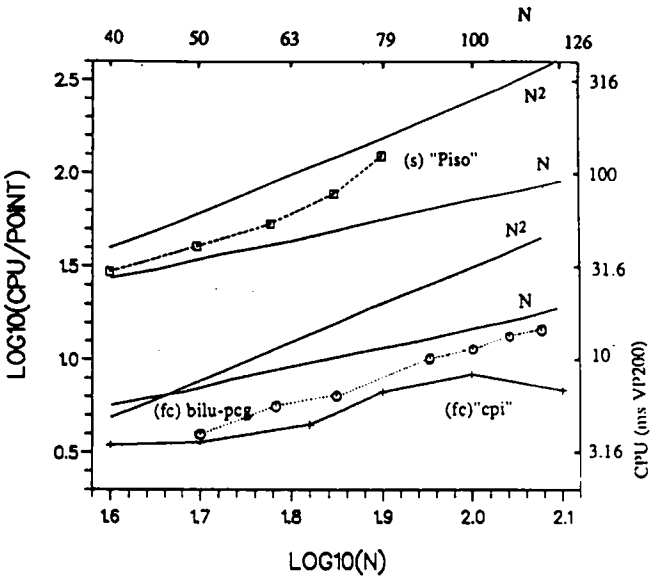

Figure 7. Square driven cavity, $Re = 400$. Evolution of computational effort with number N of points per direction: □, segregated 'PISO-like method; +, fully coupled 'CPI' method; ··· ○ ···, fully coupled ILU-PBCG method;[19] ——, evolution of CPU time per point with N or N^2 (CPU time is on VP200)

5. THE 3:1:1 LID-DRIVEN CAVITY

5.1. Presentation; grid spacing

A numerical simulation of the flow in a 3:1:1 (spanwise aspect ratio SAR = 3; see Figure 4) driven cavity $0 \leqslant x, y \leqslant 1$, $-1{\cdot}5 \leqslant z \leqslant 1{\cdot}5$ is now presented. This case is one of those considered in the experiments of References 44–46 at $Re = 3200$ and in the (still coarse grid) calculations of Reference 42. Short-survival-time Taylor-type toroidal vortices are observed soon after the lid is impulsively started. TGL vortices are present (and predicted in References 40, 42 and 43) in the fully established state. Finally, turbulence occurs for Reynolds numbers in the range from 6000 to 8000.

The simulation of three-dimensional incompressible unsteady flows is made possible with reasonable (second-order) time and spatial accuracy on presently available supercomputers. However, owing to the still high CPU cost of the method, the unsteady evolution has been studied only up to a non-dimensional time $t = 100$ with a $64 \times 64 \times 64$ grid, using a symmetry condition (in the plane $z = 0$). Preliminary calculations on a coarser $50 \times 60 \times 60$ grid indicated no spontaneous symmetry breaking, at least for $t \leqslant 100$.

5.2. Time step

An inadequate time step may also lead to erroneous results. Time step limitations may result either from numerical (stability) limitations or from physical limitations which canot be avoided with an improved numerical approach. The use of an explicit or semi-implicit approach usually imposes a (CFL-type) time step limitation depending on the grid spacing. Such a limitation may be prohibitive when a fine grid is used. The implicit fully coupled approach does not suffer from such a limitation. Nevertheless, a time step limitation still exists owing to the resolution approach for the non-linear equations. The defect correction approach and the preconditioned CG solver

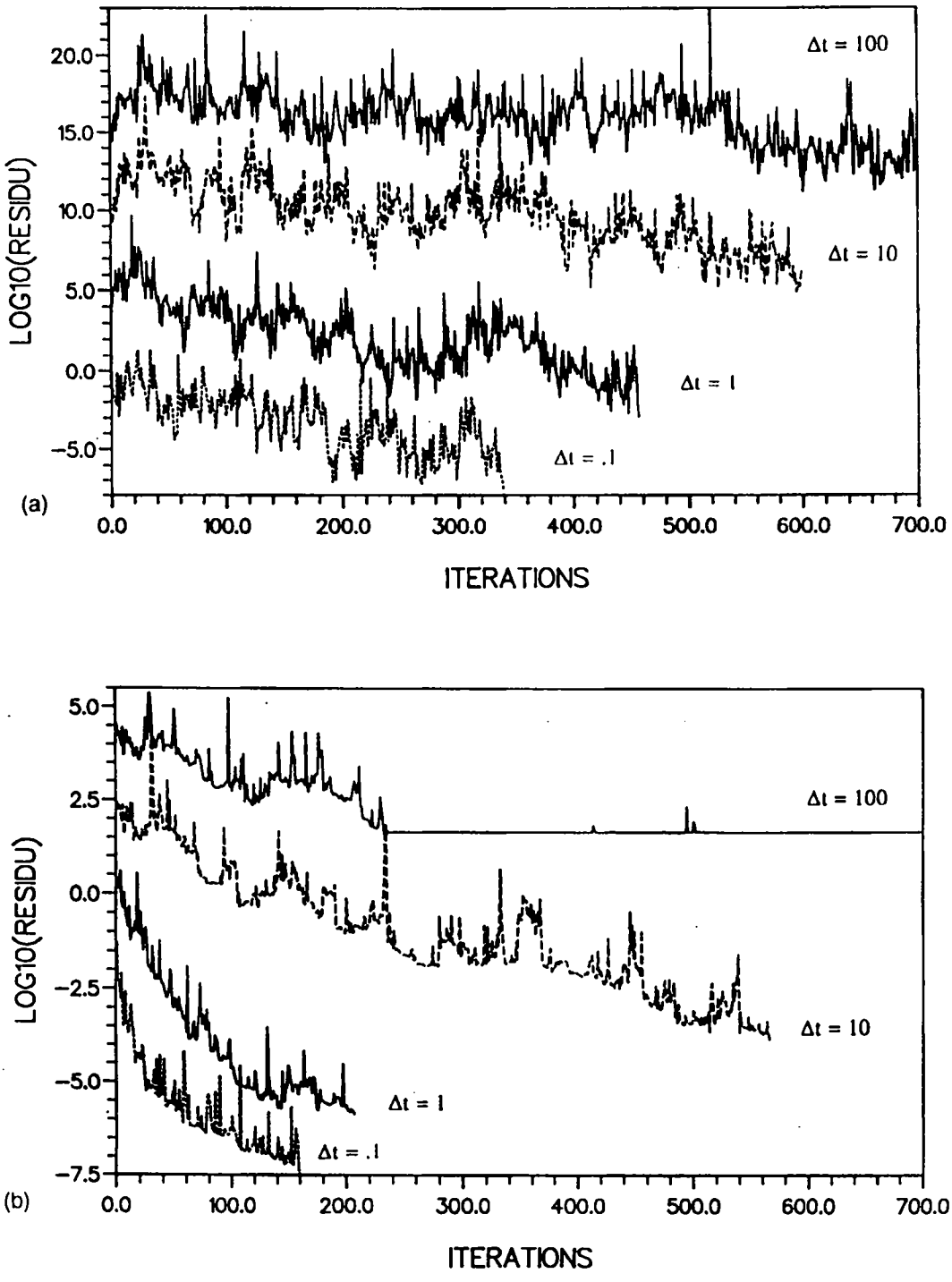

Figure 8. Three-dimensional cavity, spanwise aspect ratio (SAR) 3:1:1, $Re = 3200$, $t = 100$. Convergence history of CG methods applied to linearized equations. Preconditioning with block diagonal matrix, 50 × 50 × 60 grid. (a) 'CGS' algorithm. (b) 'CGSTAB' algorithm

allow a large-time-step simulation. However, it has been found that a converged time solution could not be obtained with a (non-dimensional) time step greater than 2. This practical limitation is believed to be due to physical reasons, since experiments[46] indicate that the developed cavity flow is quasi-periodic with a (non-dimensional) period T approximately equal to 2 (15 s).

Owing to the solenoidality constant, the total computational cost increases considerably when the time step is decreased. Convergence histories of the linearized equation for four different

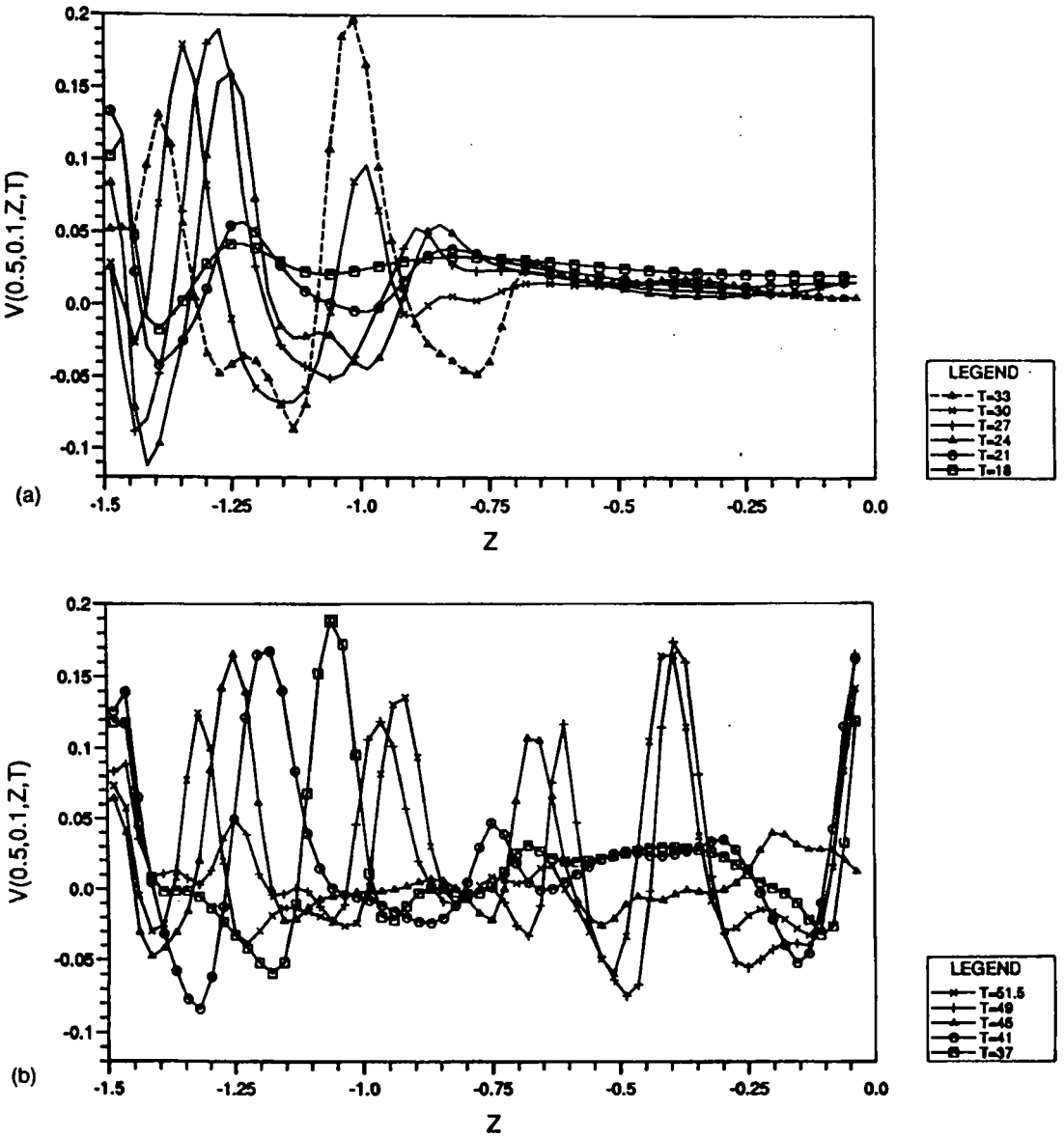

Figure 9. Three-dimensional cavity, spanwise aspect ratio (SAR) 3:1:1, $Re = 3200$. Evolution with time of selected velocity profiles $u(x, y, z)$ and $v(x, y, z)$: (a) $v(0{\cdot}5, 0{\cdot}1, z)$ for 18×33; (b) $v(0{\cdot}5, 0{\cdot}1, z)$ for $37 \leqslant t \leqslant 51{\cdot}5$

time steps ($\Delta t = 100, 10, 1, 0{\cdot}1$) at time $t = 100$ with the $50 \times 50 \times 60$ grid are compared in Figure 8(a) for 'CGS' and in Figure 8(b) for 'CGSTAB'. One can notice that 'CGSTAB' is more efficient than 'CGS' when used for time-dependent problems. The CPU time to solve the linearized system as well as the required number of non-linear iterations (not shown) are reduced when the time step is decreased, but not enough to make the total computational time independent of the used time step. Consequently, for a fully coupled implicit approach the most

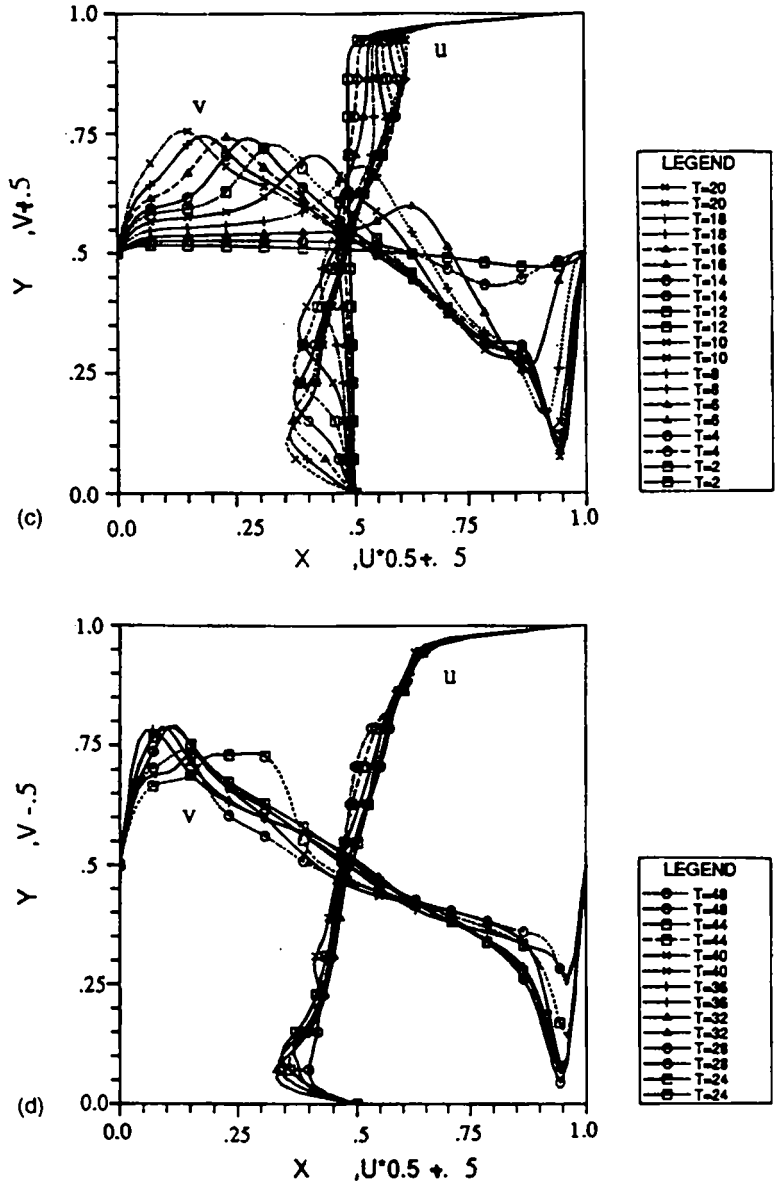

Figure 9. Three-dimensional cavity, spanwise aspect ratio (SAR) 3:1:1, $Re = 3200$. Evolution with time of selected velocity profiles $u(x, y, z)$ and $v(x, y, z)$: (c) horizontal curves, $v(x, 0{\cdot}5, 0)$ and vertical curves, $u(0{\cdot}5, y, 0)$ for $2 \leqslant t \leqslant 20$; (d) horizontal curves, $v(x, 0{\cdot}5, 0)$ and vertical curves, $u(0{\cdot}5, y, 0)$ for $24 \leqslant t \leqslant 48$

economical time step is the maximum time step allowing a good description of the physical events. As indicated previously, the lid-driven cavity flow at $Re = 3200$ tends to become periodic with a period about $T = 2$. *Thus the time step is fixed at* $\Delta t = 0{\cdot}25$ *for* $t < 50$ *while the initial phase* ($t < 50$) *is described with* $\Delta t = 0{\cdot}5$ in order to save CPU time. The computation has been performed on the CRAY2 supercomputer. The reduction factor for the residuals fo the non-linear equations is 10^3, while the residuals for the corresponding linearized equations are reduced by more than four orders of magnitude. The CPU time per point per time step is about 2·4 ms for

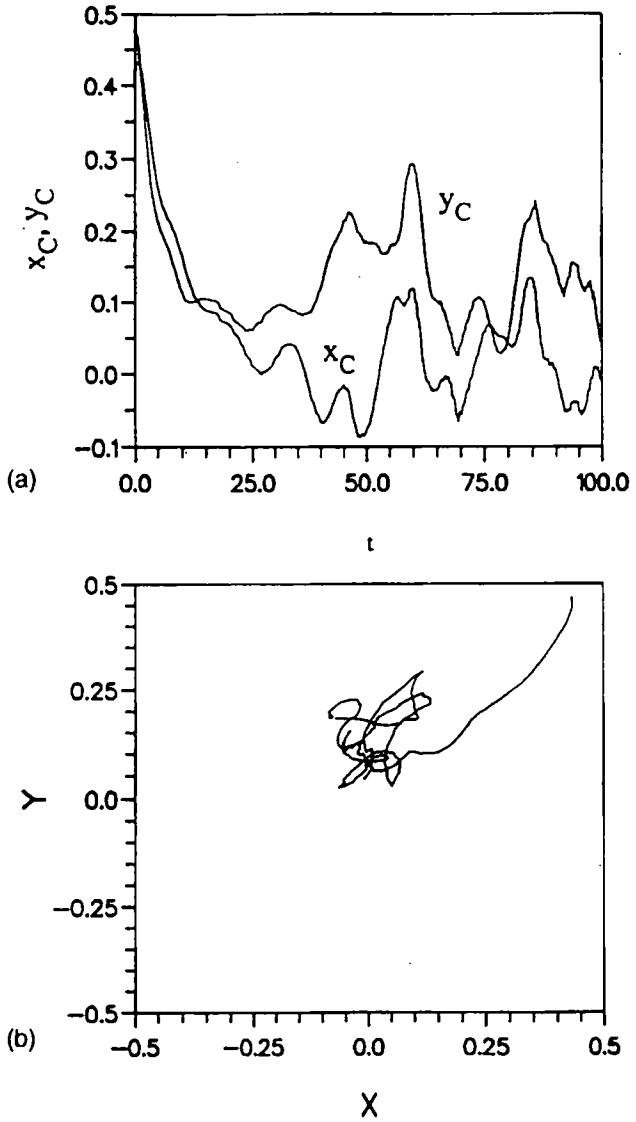

Figure 10. Impulsively started three-dimensional lid-driven cavity, spanwise aspect ratio (SAR) 3:1:1, $Re = 3200$. Evolution with time in symmetry plane $z = 0$ of primary vortex centre: (a) x_C and y_C as functions of time; trajectory of C in symmetry plane

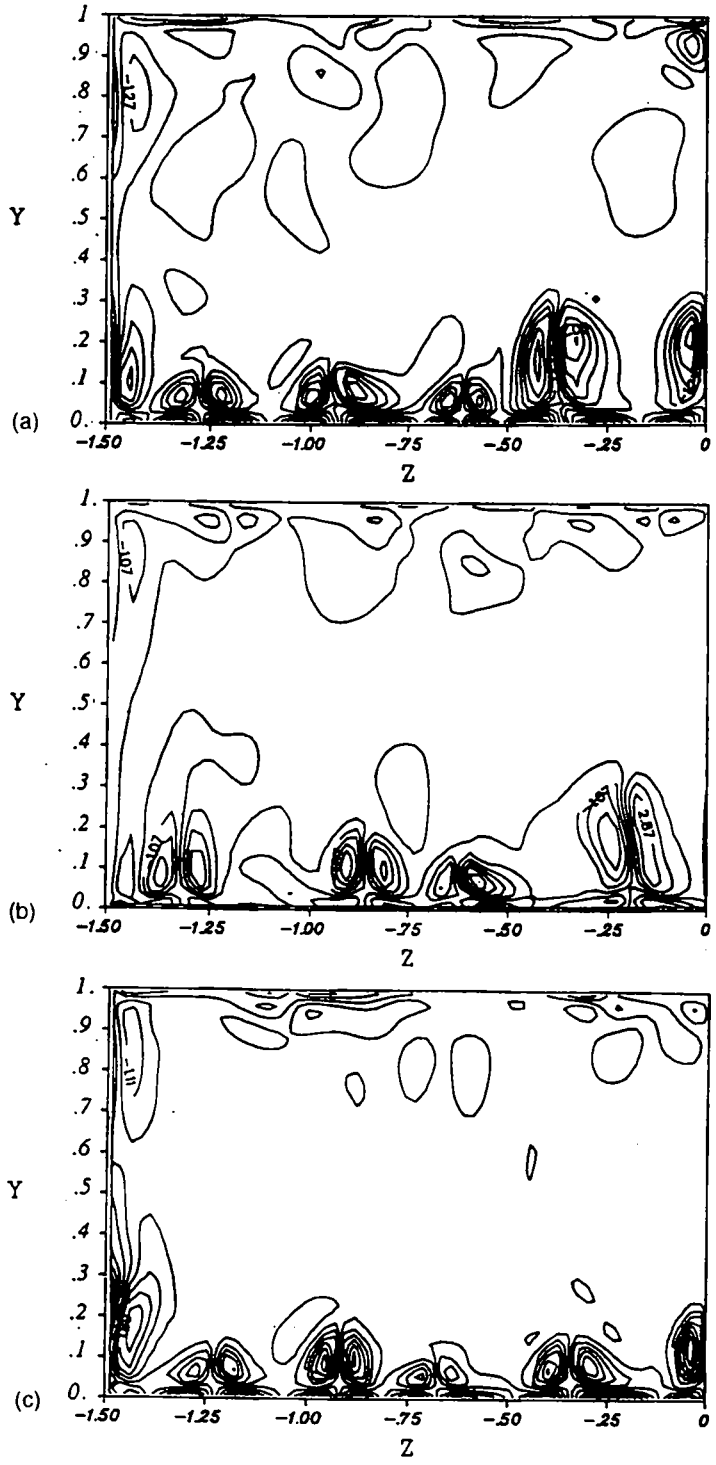

Figure 11. Impulsively started three-dimensional lid-driven cavity, spanwise aspect ratio (SAR) 3:1:1, $Re = 3200$. Contours of x-components of vorticity field in plane $x = 0$. Pattern with eight or nine pairs of TGL vortices (left, end wall; right, symmetry plane): (a) $t = 50$; (b) $t = 76$; (c) $t = 100$

$\Delta t = 0{\cdot}5$ and about 1·6 ms for $\Delta t = 0{\cdot}25$. The storage cost of the fully coupled implicit method is about 45 Mwords.

5.3. Results

To illustrate the flow evolution, four velocity profiles—$v(0{\cdot}5, 0{\cdot}1, z, t)$ and $u(0{\cdot}5, 0{\cdot}1, z, t)$ in Figures 9(a) and 9(b) and $u(0{\cdot}5, y, 0, t)$ and $v(x, 0{\cdot}5, 0, t)$ in Figures 9(c) and 9(d)—are presented. A peak in the profile $v(0{\cdot}5, 0{\cdot}1, z, t)$ indicates the presence of a pair of TGL vortices. The time evolution in the symmetry plane $z = 0$ of the primary vortex centre (x_C, y_C), identified by the location of the minimum velocity modulus, is presented in Figure 10. The birth of the primary vortex quickly follows the impulsive start of the lid. Because of the end wall, a corner vortex is formed. For, say, $t < 10$ the influence of the corner vortex is limited only to a small region close to the end wall. Unlike the experimental results where toroidal Taylor vortices were observed during the first 30 s ($t < 5$), no significant three-dimensional effect occurs except near the end wall. A simulation performed up to $t = 2$ with a smaller time step ($\Delta t = 0{\cdot}1$) gives similar results. It is unlikely that disagreement between simulation and experiment would be due to insufficient time or lack of spatial resolution. The centre of the primary vortex moves approximately along the diagonal line during this period (Figure 10(b)).

The corner vortex induces evenly distributed spanwise TGL vortices. The first pair of TGL vortices was observed around $t = 15$; it induces a second pair at about $t = 25$ (Figure 9(a)). The important 3D effect propagates from the end wall, with the TGL vortices from the end wall, and a pair of vortices centred at the symmetry plane appears at $t \approx 36$ (Figure 9(b)). The flow quickly becomes unstable in the whole cavity. The pattern of the first nine distinct pairs of TGL vortices is observed at about $t = 47$ (Figure 9(b)). Afterwards the flow is characterized by a strong interaction between the primary vortex, the TGL vortices and the corner vortices. The eight pairs that occur predominantly in the experiments of Reference 37 are observed intermittently during the simulation (Figure 11(b)), while nine pairs are most often observed, for instance at $t = 50$ (Figure 11(a)) and $t = 100$ (Figure 11(c)).

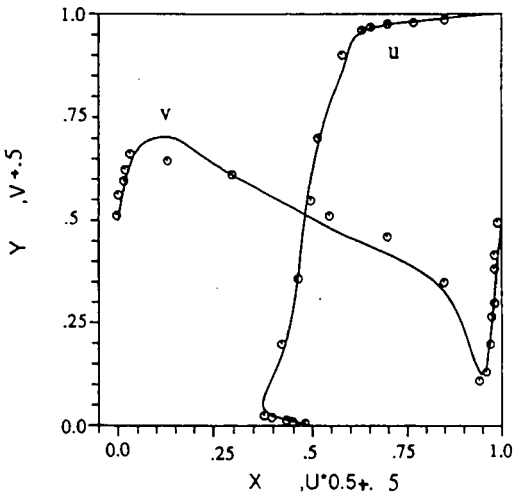

Figure 12. Impulsively started three-dimensional lid-driven cavity, spanwise aspect ratio (SAR) 3:1:1, $Re = 3200$. Time-averaged velocity profiles in symmetry plane $z = 0$ along vertical and horizontal centrelines: ——, calculated; ○, experimental

Although the existence of TGL vortices, as well as the main flow pattern, is expected to depend only on the Reynolds number, the end wall plays an important role in main flow development. The main flow is already fully developed at $t \approx 25$ (Figure 9(d)). However, the system of TGL vortices develops as a result of the interaction between the first TGL vortices propagated from the end wall and the symmetry vortices formed at $t \approx 36$ owing to the zero-flux condition. The system of TGL vortices covers the whole domain only at about $t \approx 47$ (Figure 9(b)).

Numerical mean velocity profiles at the symmetry plane for $50 < t < 100$ are compared in Figure 12 with experimental results taken in the fully established state with about 5 min sample averages (about $\Delta T = 43$). The u-velocity profile agrees well with experiments. The v-velocity profile, however, is strongly influenced by the TGL vortices and is in weaker agreement. This is probably due to the sample of numerical simulation data rather than to the grid resolution. Finally, it must be mentioned that TGL vortices influence the flow in the symmetry plane with a period which is well predicted of about 5–6 non-dimensional time units.

6. CONCLUSIONS

The new 'consistent' physical interpolation allows the use of a non-staggered grid without producing spurious pressure modes, while enforcing numerical stability and second-order accuracy. Reliable numerical results have been obtained for the 3D lid-driven cavity with a moderate grid resolution. Owing to the influence of the end wall, the TGL vortices develop in the present case without any superimposed numerical perturbation. However, the simulation has been performed only for one Reynolds number and during a short time (about 10 'physical' minutes). This is clearly not sufficient to understand the physical phenomenon in all its aspects, particularly its long-time behaviour. The simulation has to be performed over longer times and also for a larger range of Reynolds numbers.

The superiority of the fully coupled method for the iterative calculation of steady flow problems has been demonstrated. Five aspects for the superiority. (i) With a fully coupled method the iterative procedure accounting for the non-linearity becomes distinct from the problems connected to the resolution of the linear system. (ii) For steady flow problems the strength of CGS (or CGSTAB) methods provides high rates of convergence and allows quasi-infinite time steps as well. (iii) For unsteady flow problems the limitations over the size of the time step arise exclusively from the physics of the problem (presence of characteristic periods of unsteadiness); this indicates that the domain of efficiency of the fully coupled approach might be limited to flows where high-frequency unsteadiness is not too high. (iv) The evolution of the computational effort is strongly improved when the number of grid points increases. (v) There is still a serious potential for improving the global methods through the use of better preconditioners for the coupled system, perhaps by a combination of MG and CG techniques.

Among the drawbacks of the method, the use of conjugate gradient methods has to be paid for by a serious storage penalty: the required two- or three-dimensional arrays for the CG method have to be added to the two- or three-dimensional arrays needed to store the fully coupled system. It is, however, considered that this storage penalty is a very weak drawback with respect to the increased efficiency and robustness of the fully coupled method.

ACKNOWLEDGEMENTS

The authors gratefully acknowledge partial financial support of DRET through Contracts 89-117 and 92.046 and support of the GdR 'Mécanique des Fluides Numérique' (CNRS). Computations have been performed on the CRAY2 (CCVR) with CPU provided by the Scientific Committee of CCVR and on the VP200 (CIRCE) with CPU provided by the DS of SPI.

APPENDIX I: CLOSURE RELATIONSHIPS

We may introduce

$$D_e = \frac{\max(u_e^*, 0)}{h_x} + \frac{\max(-u_e^*, 0)}{h_x} + \frac{\max(v_e^*, 0)}{H_y} + \frac{\max(-v_e^*, 0)}{H_y} + \frac{2}{Reh_x^2} + \frac{3}{2\Delta t}.$$

Then the non-vanishing coefficients of (13) are

$$C_{eC} = \frac{1}{D_e}\left(\frac{\max(u_e^*, 0)}{h_x} + \frac{1}{Reh_x^2} - \frac{1}{ReH_y^2}\right),$$

$$C_{eE} = \frac{1}{D_e}\left(\frac{\max(-u_e^*, 0)}{h_x} + \frac{1}{Reh_x^2} - \frac{1}{ReH_y^2}\right),$$

$$C_{eN} = C_{eNE} = \frac{1}{D_e H_y}\left(\frac{\max(-v_e^*, 0)}{2} + \frac{1}{2ReH_y^2}\right),$$

$$C_{eS} = C_{eSE} = \frac{1}{D_e H_y}\left(\frac{\max(v_e^*, 0)}{2} + \frac{1}{2ReH_y^2}\right),$$

$$B_{eC}^u = -B_{eE}^u = \frac{1}{D_e H_x},$$

so that

$$u_e = \hat{u}_e + B_{eC}^u(P_C - P_E) + g_e^u,$$

with

$$\hat{u}_e = C_{eC}U_C + C_{eE}U_E + C_{eN}(U_N + U_{NE}) + C_{eS}(U_S + U_{SE}), \qquad g_e^u = (4u_e^n - u_e^{n-1})/2\Delta t.$$

As indicated, $\hat{u}_e$ involves nodes C, N, E, S and NE, SE for U and nodes C and E for P. It can be noticed that $C_{eC} + C_{eE} + C_{eN} + C_{eNE} + C_{eS} + C_{eSE} = 1 - 3/2D_e\Delta t$, so that the closure relationship interpolates between the nodal values. However, the interpolation is not necessarily monotonic, since coefficients C_{eC} and C_{eE} may become negative.

The term v_e is obtained in the same way from the convective form of the V-momentum equation where the pressure gradient is approximated as

$$\left.\frac{\partial P}{\partial y}\right|_e \approx \tfrac{1}{4}H_y(P_N + P_{NE}) - \tfrac{1}{4}H_y(P_S + P_{SE}),$$

i.e.

$$v_e = \hat{v}_e + B_{eN}^v(P_N + P_{NE}) + B_{eC}^v(P_C + P_E) + B_{eS}^v(P_S + P_{SE}) + g_e^v,$$

with

$$\hat{v}_e = C_{eC}V_C + C_{eE}V_E + C_{eN}(V_N + V_{NE}) + C_{eS}(V_S + V_{SE}), \qquad g_e^v = (4v_e^n - v_e^{n-1})/2\Delta t,$$

where coefficients C_{eC}, C_{eE}, C_{eN} and C_{eS} are defined as before, while now

$$B^v_{eN} = B^v_{eNE} = -\frac{1}{4D_e H_y}, \qquad B^v_{eC} = B^v_{eE} = 0, \qquad B^v_{eS} = B^v_{eSE} = \frac{1}{4D_e H_y}.$$

For the sake of conciseness, similar relations for u and v at points n, w, s are omitted. They are easily obtained in the same way as u_e and v_e.

APPENDIX II: INFLUENCE COEFFICIENTS

Influence coefficients of P in the pressure equation:

$$K^{pp}_C = H_y(B^u_{eC} + B^u_{wC}) + H_x(B^v_{nC} + B^v_{sC}),$$

$$K^{pp}_E = -H_y B^u_{eC}, \qquad K^{pp}_W = -H_y B^u_{wC}, \qquad K^{pp}_N = -H_x B^v_{nC}, \qquad K^{pp}_S = -H_x B^v_{sC}.$$

Influence coefficients of U and V in the pressure equation:

$$K^{pu}_C = H_y(C_{eC} - C_{wC}), \quad K^{pu}_N = H_y(C_{eN} - C_{wN}), \quad K^{pu}_S = H_y(C_{eS} - C_{wS}), \quad K^{pu}_E = H_y C_{eE},$$

$$K^{pu}_W = -H_y C_{wW}, \quad K^{pu}_{NE} = H_y C_{eN}, \quad K^{pu}_{NW} = -H_y C_{wN}, \quad K^{pu}_{SE} = H_y C_{eS}, \quad K^{pu}_{SW} = -H_y C_{wS},$$

$$K^{pv}_C = H_x(C_{nC} - C_{sC}), \quad K^{pv}_E = H_x(C_{nE} - C_{sE}), \quad K^{pv}_W = H_x(C_{nW} - C_{sW}), \quad K^{pv}_N = H_x C_{nN},$$

$$K^{pv}_S = -H_x C_{sS}, \quad K^{pv}_{NE} = H_x C_{nE}, \quad K^{pv}_{NW} = H_x C_{nW}, \quad K^{pv}_{SE} = -H_x C_{sE}, \quad K^{pv}_{SW} = -H_x C_{sW}.$$

Influence coefficients of P in the U-momentum equation:

$$K^{up}_C = H_y(u^*_e B^u_{eC} + u^*_w B^u_{wC}) + H_x(v^*_n B^u_{nC} + u^*_s B^u_{sC}), \quad K^{up}_N = H_x V^*_n B^u_{nC}, \quad K^{up}_S = -H_x v^*_s B^u_{sC},$$

$$K^{up}_E = H_x\left(v^*_n B^u_{nE} - v^*_s B^u_{sE} + \frac{H_y}{2H_x}\right) - H_y u^*_e B^u_{eC}, \quad K^{up}_{NE} = H_x v^*_n B^u_{nE}, \quad K^{up}_{SE} = -H_x v^*_s B^u_{sS},$$

$$K^{up}_W = H_x\left(v^*_n B^u_{nW} - v^*_s B^u_{sW} - \frac{H_y}{2H_x}\right) - H_y u^*_w B^u_{wC}, \quad K^{up}_{NW} = H_x v^*_n B^u_{nW}, \quad K^{up}_{SW} = -H_x v^*_s B^u_{sW}.$$

Influence coefficients of P in the V-momentum equation:

$$K^{vp}_C = H_x(v^*_n B^v_{nC} + v^*_s B^v_{sC}) + H_y(u^*_e B^v_{eC} + v^*_w B^v_{wC}), \quad K^{vp}_E = H_y u^*_e B^v_{eC}, \quad K^{vp}_W = -H_y u^*_w B^v_{wC},$$

$$K^{vp}_N = H_y\left(u^*_e B^v_{eN} - u^*_w B^v_{wN} + \frac{H_x}{2H_y}\right) - H_x v^*_n B^v_{nC}, \quad K^{vp}_{NE} = H_y u^*_e B^v_{eN}, \quad K^{vp}_{NW} = -H_y u^*_w B^v_{wN},$$

$$K^{vp}_S = H_y\left(u^*_e B^v_{eN} - u^*_w B^v_{wS} - \frac{H_x}{2H_y}\right) - H_x v^*_s B^v_{sC}, \quad K^{vp}_{SE} = H_y u^*_e B^v_{eS}, \quad K^{vp}_{SW} = -H_y u^*_w B^u_{wS}.$$

Influence coefficients of U in the U-momentum equation are identical with corresponding influence coefficients of V in the V-momentum equation. The values are

$$K_C^{uu} = H_y\left(C_{eC}u_e^* - C_{wC}u_w^* + \frac{2}{ReH_x}\right) + H_x\left(C_{nC}v_n^* - C_{sC}v_S^* + \frac{2}{ReH_y}\right),$$

$$K_N^{uu} = H_y(C_{eN}u_e^* - C_{wN}u_w^*) + H_x\left(C_{nN}v_n^* - \frac{1}{ReH_y}\right),$$

$$K_S^{uu} = H_y(C_{eS}u_e^* - C_{wS}u_w^*) - H_x\left(C_{sS}v_S^* + \frac{1}{ReH_y}\right),$$

$$K_E^{uu} = H_x(C_{nE}v_n^* - C_{sE}v_S^*) + H_y\left(C_{eE}u_e^* - \frac{1}{ReH_x}\right),$$

$$K_W^{uu} = H_x(C_{nW}v_n^* - C_{sW}v_S^*) - H_y\left(C_{wW}u_W^* + \frac{1}{ReH_x}\right),$$

$$K_{NE}^{uu} = H_yC_{eN}u_e^* + H_xC_{nE}v_n^*, \qquad K_{SE}^{uu} = H_yC_{eS}u_e^* - H_xC_{sE}v_S^*,$$

$$K_{NW}^{uu} = -H_yC_{wN}u_W^* + H_xC_{nW}v_n^*, \qquad K_{SW}^{uu} = -H_yC_{wS}u_w^* - H_xC_{sw}v_S^*.$$

Known source terms:

$$g_C^u = H_y(u_e^*g_e^u - u_w^*g_w^u) + H_x(v_n^*g_n^u - v_s^*g_s^u), \qquad g_C^v = H_y(u_e^*g_e^v - u_w^*g_w^v) + H_x(v_n^*g_n^v - v_s^*g_s^v),$$

$$f^u = \frac{e_1}{3}(4U_C^n - U_C^{n-1}) - g_C^u, \qquad f^v = \frac{e_1}{3}(4V_C^n - V_C^{n-1}) - g_C^v, \qquad e_1 = 3H_xH_y/2\Delta t.$$

APPENDIX III

The fully-coupled system: the ijth 3×3 block row of **A** such that **AX** = **B** is

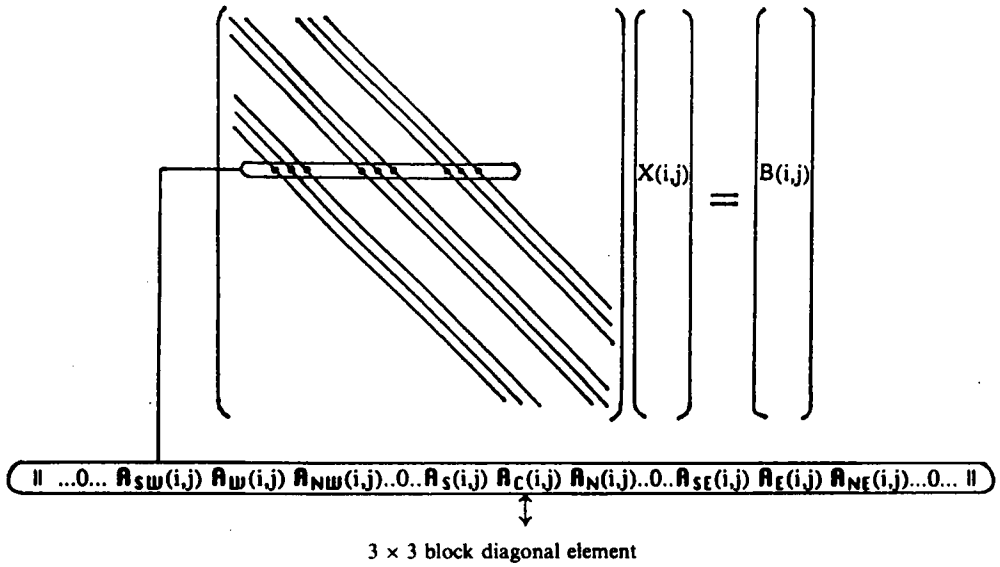

The block diagonal element corresponding to the element $\mathbf{X}(i, j)$:

$$\mathbf{A}_C(i, j) \equiv \begin{pmatrix} e_1 + K_C^{uu} & 0 & -K_C^{up} \\ 0 & e_1 + K_C^{uu} & -K_C^{vp} \\ K_C^{pu} & K_C^{pv} & K_C^{pp} \end{pmatrix}(i, j).$$

The block element corresponding to the unknown $\mathbf{X}(i, j + 1)$:

$$\mathbf{A}_N(i, j) \equiv \begin{pmatrix} -K_N^{uu} & 0 & -K_N^{up} \\ 0 & -K_N^{uu} & -K_N^{vp} \\ K_N^{pu} & K_N^{pv} & K_N^{pp} \end{pmatrix}(i, j).$$

The value of other coefficients is obtained by substituting to N other neighbours. The right-hand side corresponding to the known vector $\mathbf{b}_C(i, j)$:

$$\mathbf{b}_C(i, j) \equiv \| f^u, f^v, f^p \|^T(i, j).$$

Note: The value of coefficients K and of f^u, f^v are those given in Appendix II.

APPENDIX IV: BiCG, CGS AND BiCGSTAB METHODS

The most common so-called Krylov subspace method for solving the linear system $\mathbf{Ax} = \mathbf{b}$ is the biconjugate gradient method (BiCG), which constructs non-optimal approximations in the so-called Krylov subspace $\mathbf{x}^k \in \mathbf{x}^0 + \text{span}(\mathbf{r}^0, \mathbf{Ar}^0, \ldots, \mathbf{A}^{k-1}\mathbf{r}^0)$ such that the error vector $\boldsymbol{\varepsilon}^k = \mathbf{x}^k - \mathbf{x}$ satisfies $\boldsymbol{\varepsilon}^k = p_k(\mathbf{A})\boldsymbol{\varepsilon}^0$ and $\mathbf{r}^k = p_k(\mathbf{A})\mathbf{r}^0$ for some polynomial p_k of degree k. Here $\mathbf{r}^k = \mathbf{b} - \mathbf{Ax}^k$, $k = 0, \ldots$, is the residual; p_k is determined from the orthogonality condition

$$\mathbf{r}^k \perp (\mathbf{s}^0, \mathbf{As}^0, \ldots, \mathbf{A}^{k-1}\mathbf{s}^0), \quad \text{where } \mathbf{s}^0 = \mathbf{r}^0, \quad \text{while } s^k \perp (\mathbf{r}^0, \mathbf{Ar}^0, \ldots, \mathbf{A}^{k-1}\mathbf{r}^0).$$

This BiCG method is not optimal in that $\|\mathbf{r}^k\|$ is not minimized, but it computes $\mathbf{x}^k$ using two three-term recurrence relations for $\{\mathbf{r}_k\}$ and $\{\mathbf{s}_k\}$. Hence it is less costly and less storage-consuming per iteration than a Krylov subspace method which minimizes the residual. The BiCG method terminates within n steps at most (in exact arithmetic) and is coded as follows.

(1) *Start.*
- *Choose* $\mathbf{x}_0$ *and* $\mathbf{s}_0 \neq \mathbf{0}$, *for instance* $\mathbf{s}_0 = \mathbf{r}_0$, *such that* $\mathbf{s}_0^T \cdot \mathbf{r}_0 \neq 0$.
- *Set* $\mathbf{p}_0 = \mathbf{q}_0 = 0$; $\rho_0 = 1$.

(2) *For* $k = 1, 2, \ldots$ *do*:
- *Compute* $\rho_k = \mathbf{s}_{k-1}^T \cdot \mathbf{r}_{k-1}$.
- $\beta_k = \rho_k / \rho_{k-1}$.
- $\mathbf{p}_k = \mathbf{r}_{k-1} + \beta_k \mathbf{p}_{k-1}$—first residual update.
- $\mathbf{q}_k = \mathbf{s}_{k-1} + \beta_k \mathbf{q}_{k-1}$—second residual update.
- $\alpha_k = \rho_k / \mathbf{q}_k^T \cdot \mathbf{Ap}_k$.
- $\mathbf{x}_k = \mathbf{x}_{k-1} + \alpha_k \mathbf{p}_k$.

(3) *If* $\mathbf{x}_k$ *accurate enough, then quit.*

Else:
- $\mathbf{r}_k = \mathbf{r}_{k-1} - \alpha_k \mathbf{Ap}_k$ (rather than $\mathbf{r}_k = \mathbf{b} - \mathbf{Ax}_k$).
- $\mathbf{s}_k = \mathbf{s}_{k-1} - \alpha_k \mathbf{A}^T \mathbf{q}_k$.

End.

Sonneveld[24] observed that $\{\mathbf{r}_k\}$ and $\{\mathbf{s}_k\}$ converge to zero but that only the convergence of $\{\mathbf{r}_k\}$ is exploited. He showed that vectors $\{\mathbf{s}_k\}$ need not be solved and multiplication by $\mathbf{A}^T$ can be avoided. Sonneveld has reorganized BiCG, accounting for the fact that one can replace $\boldsymbol{\varepsilon}^k = p_k(\mathbf{A})\boldsymbol{\varepsilon}^0$ and $\mathbf{r}^k = p_k(\mathbf{A})\mathbf{r}^0$ by

$$\boldsymbol{\varepsilon}^k = p_k^2(\mathbf{A})\boldsymbol{\varepsilon}^0 \quad \text{and} \quad \mathbf{r}^k = p_k^2(\mathbf{A})\mathbf{r}^0$$

for the same polynomial p_k, with no increase in the amount of work per step and with a convergence (or divergence) faster than for BiCG by a factor of between one and two. Moreover, while BiCG requires vector multiplications by both A and $\mathbf{A}^T$, CGS requires only multiplications by A as indicated by the following procedure.

(1) *Start.*
- *Choose* x^0 *and* $\mathbf{s}_0 \neq \mathbf{0}$, *for instance* $\mathbf{s}_0 = \mathbf{r}^0$.
- *Set* $\mathbf{p}_0 = \mathbf{q}_0 = 0$; $\rho_0 = 1$ *and compute* $\mathbf{s}_0^T \cdot \mathbf{r}^0 \neq 0$.

(2) *For* $k = 1, 2, \ldots$ *do*:
- *Compute* $\rho_k = \mathbf{s}_0^T \cdot \mathbf{r}^{k-1}$.
- $\beta_k = \rho_k / \rho_{k-1}$.
- $\mathbf{u}_k = \mathbf{r}_k + \beta_k \mathbf{q}_{k-1}$.
- $\mathbf{p}_k = \mathbf{u}_k + \beta_k(\mathbf{q}_{k-1} + \beta_k \mathbf{p}_{k-1})$.
- *Solve* y *from* $\mathbf{My} = \mathbf{p}_k$.
- $\alpha_k = \rho_{k-1} / \mathbf{s}_0^T \cdot \mathbf{Ay}$.
- $\mathbf{q}_k = \mathbf{u}_k - \alpha_k \mathbf{Ay}$.
- Solve z *from* $\mathbf{Mz} = \mathbf{u}_k + \mathbf{q}_k$.
- $\mathbf{x}^k = \mathbf{x}^{k-1} + \alpha_k \mathbf{z}$.
- $\mathbf{r}^k = \mathbf{r}^{k-1} - \alpha_k \mathbf{Az}$ (rather than $\mathbf{r}^k = \mathbf{b} - \mathbf{Ax}^k$).

(3) *If* $\mathbf{x}^k$ *accurate enough, then quit.*

End.

It may take far more iteration steps for a true residual process to get at an $\mathbf{x}_k$ of similar accuracy as in the CGS algorithm in the form given: CGS may even converge, while the true residual process does not. This is probably because locally large variations in a current update direction overshadow variations in other almost converged directions, so that the true residual vector does not necessarily satisfy the underlying orthogonality relations for the updated vectors $\mathbf{P}_k(\mathbf{A})\mathbf{r}_0$. Finally, far from converging monotonically, CGS is susceptible to breakdown if $\rho_{k-1} = 0$ at some step. It is in principle possible to avoid exact breakdowns, but we have not studied this question since breakdown never occurred in treated problems.

The CGS procedure as presented involves the preconditioning matrix $\mathbf{M} = \mathbf{K}_1\mathbf{K}_2$, so that the 'primitive' system $\mathbf{Ax} = \mathbf{b}$ is supplied by $\bar{\mathbf{A}}\bar{\mathbf{x}} = \bar{\mathbf{b}}$, where $\bar{\mathbf{A}} = \mathbf{K}_1^{-1}\mathbf{A}\mathbf{K}_2^{-1}$, $\mathbf{x} = \mathbf{K}_2^{-1}\bar{\mathbf{x}}$ and $\mathbf{b} = \mathbf{K}_1^{-1}\bar{\mathbf{b}}$. In the case of Jacobi (left) preconditioning, $\mathbf{K}_1 = \mathbf{D}$ (= diag(A)) and $\mathbf{K}_2 = \mathbf{I}$. In the case of an incomplete LU preconditioning, $\mathbf{K}_1 = \mathbf{L}$ and $\mathbf{K}_2 = \mathbf{U}$. Instead of solving linear systems based on A, one has to solve the 'easier' system $\mathbf{My} = \mathbf{c}$ for $\mathbf{c} = \mathbf{p}_k$ and $\mathbf{c} = \mathbf{u}_k + \mathbf{q}_k$ for each k during the *do*-loop (2). It is remarkable to notice that $\mathbf{K}_1$ and $\mathbf{K}_2$ play no explicit role in the CGS procedure and that any of the forms of preconditioning corresponds only with a different choice for $\mathbf{s}_0$ in the unpreconditioned system.

With a slight modification of the aforementioned algorithms, the decrease in residuals can be made more regular.[25] The resulting procedure (BiCGSTAB) is as follows.

(1) *Start.*
- *Choose* $\mathbf{x}_0$ *and* $\mathbf{s}_0 \neq \mathbf{0}$, *for instance* $\mathbf{s}_0 = \mathbf{r}_0$.
- *Set* $\mathbf{v}_0 = \mathbf{p}_0 = \mathbf{q}_0 = 0$; $\rho_0 = \alpha_0 = \omega_0 = 1$.

(2) *For* $k = 1, 2, \ldots$ *do*:
- *Compute* $\rho_k = \mathbf{s}_0^T \cdot \mathbf{r}_{k-1}$.
- $\beta_k = \alpha_{k-1}\rho_k/(\omega_{k-1}\rho_{k-1})$.
- $\mathbf{p}_k = \mathbf{r}_{k-1} + \beta_k(\mathbf{p}_{k-1} - \omega_{k-1}\mathbf{v}_{k-1})$—first residual update.
- *Solve* $\mathbf{y}$ *from* $\mathbf{My} = \mathbf{p}_k$.
- $\alpha_k = \rho_k/\mathbf{s}_0^T \cdot \mathbf{Ay}$.
- $\mathbf{q}_k = \mathbf{r}_{k-1} - \alpha_k \mathbf{Ay}$—second residual update.
- *Solve* $\mathbf{z}$ *from* $\mathbf{Mz} = \mathbf{q}_k$.
- $\omega_k = [(\mathbf{K}_1^{-1}\mathbf{Az})^T \cdot \mathbf{K}_1^{-1}\mathbf{q}_k]/[(\mathbf{K}_1^{-1}\mathbf{Az})^T \cdot \mathbf{K}_1^{-1}\mathbf{Az}]$.
- $\mathbf{x}_k = \mathbf{x}_{k-1} + \alpha_k \mathbf{y} + \omega_k \mathbf{z}$.

(3) *If* $\mathbf{x}_k$ *accurate enough, then quit.*
- $\mathbf{r}_k = \mathbf{q}_k - \omega_k \mathbf{Az}$ (rather than $\mathbf{r}_k = \mathbf{b} - \mathbf{Ax}_k$).

End.

Updates to the current solution are carried out in a single step, while the updates on the residuals are done separately. $\mathbf{q}_k$ is the residual after the BiCG step. A variant of the BiCGSTAB algorithm moves the computation of $\mathbf{r}_k$ in the initialization part into the form *compute* $\rho_1 = \mathbf{s}_0^T \cdot \mathbf{r}_0 \neq 0$ and it includes after the computation of ω_k, $\rho_{k+1} = -\omega_k \mathbf{s}_0^T \cdot \mathbf{Aq}_k$. In contrast with CGS, $\mathbf{K}_1$ is seen to play an explicit role in the preconditioned CGSTAB method.

Since $(\mathbf{P}_i(\mathbf{A})\mathbf{s}_0, \mathbf{Q}_j(\mathbf{A}^T)\mathbf{s}_0 = 0$ for $j < i$, BiCGSTAB is a finite method: $q_N = 0$ and ω_N is undefined. Apart from preconditioning, CGS and BiCGSTAB require four additional N-vectors: $\mathbf{s}_0$, $\mathbf{p}_0$, $\mathbf{Ap}_k$, $\mathbf{Aq}_k$ ($\mathbf{r}_k$ is overwritten by $\mathbf{q}_k$). BiCGSTAB requires two images, $12N$ flops for vector updates and four inner products; CGS requires two images, $13N$ flops for vector updates and two inner products. Hence the CPU costs are comparable. Again breakdown (due to $\omega_{k-1} = 0$ *or* $\rho_{k-1} = 0$) never occurred in the cases treated so far.

APPENDIX V: DETERMINATION OF THE PRESUMED ACCURACY

According to the Taylor series expansion of a numerical scheme, a numerical solution can be approximated by

$$U_h = U_{ex} + Ch^\alpha, \tag{25}$$

where U_h is the computed approximate solution and U_{ex} is the (unknown) exact solution of the differential problem. Parameters C and α, the presumed order of accuracy, are constants to determine; h is a given available measure of the grid spacing. While all norm spacings are equivalent on a uniform grid, they are not on a non-uniform grid. In the latter case h is a local measure of the grid at a given point. We suppose that we have computed the numerical solution with three grids of grid spacing measures h_1, h_2, h_3:

$$U_{h_1} = U_{ex} + Ch_1^\alpha, \qquad U_{h_2} = U_{ex} + Ch_2^\alpha, \qquad U_{h_3} = U_{ex} + Ch_3^\alpha. \tag{26}$$

The three unknowns C, α and U_{ex} can be easily determined from (26). The order of accuracy α can be obtained iteratively using

$$\alpha = \frac{\ln[A(h_2/h_1)^\alpha - A + 1]}{\ln(h_3/h_1)}, \quad \text{where } A = \frac{U_{h_3} - U_{h_1}}{U_{h_2} - U_{h_1}}. \tag{27}$$

The constant C results from

$$C = \frac{U_{h_2} - U_{h_1}}{h_2^\alpha - h_1^\alpha}. \tag{28}$$

Hence

$$U_{ex} = U_{h_1} - Ch_1^\alpha. \tag{29}$$

REFERENCES

1. S. V. Patankar, *Numerical Heat Transfer and Fluid Flow*, McGraw-Hill, New York, 1980.
2. R. I. Issa, 'Solution of the implicitly discretized fluid flow equations by operator-splitting', *J. Comput. Phys.*, **62**, 40–65 (1986).
3. J. Piquet and M. Visonneau, 'Computation of the flow past a shiplike hull', *Comput. Fluids*, **19**, 183–215 (1991).
4. L. S. Caretto, R. M. Curr and D. B. Spalding, 'A calculation procedure for heat, mass and momentum transfer in three-dimensional parabolic flows', *Int. J. Heat Mass Transfer*, **15**, 1878–1806 (1972).
5. M. Hoekstra, 'Recent developments in a ship stern flow prediction code', in K. H. Mori (ed.), *Proc. 5th Symp. on Numerical Ship Hydrodynamics*, Hiroshima, 1989, pp. 87–101.
6. S. P. Vanka, 'Block-implicit multigrid solution of Navier–Stokes equations in primitive variables', *J. Comput. Phys.*, **65**, 138–158 (1986).
7. C. H. Bruneau and C. Jouron, 'An efficient scheme for solving steady incompressible Navier–Stokes equations', *J. Comput. Phys.*, **89**, 389–413 (1990).
8. C. Arakawa, A. O. Demuren, W. Rodi and B. Schönung, 'Application of multigrid methods for the coupled and decoupled solution of the incompressible Navier–Stokes equations', in M. Deville (ed.), *Notes on Numerical Fluid Mechanics*, Vol. 20, *Proc. 7th GAMM Conf. on Numerical Methods in Fluid Mechanics*, Vieweg, Braunschweig, 1987, pp. 1–7.
9. J. Linden, G. L. Lonsdale, B. Steckel and K. Stüben, 'Multigrid for the steady-state incompressible Navier–Stokes equations: a survey', *GMD Arbeitspapier 322*, 1988.
10. G. E. Schneider and M. Zedan, 'A coupled modified strongly implicit procedure for the numerical solution of coupled continuum problem', *AIAA Paper 84-1743*, 1984.
11. C. M. Rhie and W. L. Chow, 'A numerical study of the turbulent flow past an isolated airfoil with trailing edge separation', *AIAA J.*, **21**, 1525–1532 (1983).
12. M. E. Braaten and W. Shyy, 'Comparison of iterative and direct solution methods for viscous flow calculations in body-fitted co-ordinates', *Int. j. numer. methods fluids*, **6**, 325–349 (1986).
13. S. C. Eisenstat, M. C. Gursky, M. H. Schulz and A. H. Sherman, 'Yale sparse matrix package, II. The nonsymmetric codes', *Res. Rep. 114*, Department of Mechanical Engineering, Yale University, 1977.
14. K. C. Karki and H. C. Mongia, 'Evaluation of a coupled solution approach for fluid flow calculation in body-fitted coordinates', *Int. j. numer. methods fluids*, **11**, 1–20 (1990).
15. J. W. MacArthur and S. V. Patankar, 'Robust semi-direct finite-difference methods for solving the Navier–Stokes and energy equations', *Int. j. numer methods fluids*, **9**, 325–340 (1990).
16. W. G. Habashi, M. F. Peeters, M. P. Robichaud and V. N. Nguyen, 'Finite element algorithm for incompressible Navier–Stokes equations', in M. D. Gunzburger and R. A. Nicolaides (eds.), *Incompressible Computational Fluid Dynamics, Trends and Advances*, Cambridge University Press, Cambridge, 1993, pp. 151–182.
17. M. Peric, R. Kessler and G. Scheuerer, 'Comparison of finite-volume numerical methods with staggered and colocated grids', *Comput. Fluids*, **16**, 389–403 (1988).
18. G. B. Deng, J. Piquet, P. Queutey and M. Visonneau, 'Three-dimensional full Navier–Stokes solvers for incompressible flows past arbitrary geometries', *Int. numer. methods eng.*, **31**, 1427–1451 (1991).
19. G. B. Deng, J. Piquet and M. Visonneau, 'Viscous flow computations using a fully-coupled technique', *Proc. 2nd Int. Colloq. on Viscous Fluid Dynamics in Ship and Ocean Technology*, Osaka, 1991.
20. G. E. Schneider and M. J. Raw, 'Control-volume finite element method for heat transfer and fluid flow using colocated variables', *Numer Heat Transfer*, **11**, 363–400 (1987).
21. B. W. Char, K. O. Geddes, G. H. Gonnet, B. Leong, M. B. Monagan and S. M. Watt, *First Leaves: A Tutorial Introduction to Maple V*, Springer, New York, 1992.
22. J. Piquet and P. Queutey, 'Navier–Stokes computations past a prolate spheroid at incidence. II: High incidence case', *Int. j. numer. methods fluids*, **16**, 1–27 (1993).
23. G. B. Deng, M. Ferry, J. Piquet, P. Queutey and M. Visonneau, 'New fully-coupled solutions of the Navier–Stokes equations', in L. L. Ryhming (ed.), *Notes on Numerical Fluid Mechanics*, Vol. 35, *Proc. 9th GAMM Conf.*, Vieweg, Braunschweig, 1992, pp. 191–200.
24. P. Sonneveld, 'CGS: a fast Lanczos-type solver for non symmetric linear systems', *SIAM J. Sci. Stat. Comput.*, **10**, 36–52 (1989).

25. H. A. Van der Vorst, 'BI-CGSTAB: a fast and smoothly converging variant of Bi-CG for the solution of nonsymmetric linear systems', *SIAM J. Sci. Stat. Comput.*, **13**, 631–644 (1990).
26. U. Ghia, K. N. Ghia and C. T. Shin, 'High-Re solution for incompressible flow using the Navier–Stokes equations and multigrid method', *J. Comput. Phys.*, **48**, 387–411 (1982).
27. C. J. Chen and H. J. Chen, 'Finite analytic numerical method for unsteady two-dimensional Navier–Stokes equations', *J. Comput. Phys.*, **53**, 209–226 (1984).
28. H. Takami and K. Kuwahara, 'Numerical study of three-dimensional flow within a cubic cavity', *J. Phys. Soc. Jpn.*, **37**, 1695–1698 (1974).
29. G. De Vahl Davis and G. D. Mallinson, 'An evaluation of upwind and central difference approximations by a study of recirculating flow', *Comput. Fluids*, **4**, 29–43 (1976).
30. T. Goda, 'A multistep technique with implicit difference schemes for calculating two or three-dimensional cavity flows', *J. Comput. Phys.*, **30**, 76–95 (1979).
31. S. C. R. Dennis, D. B. Ingham and P. N. Cook, 'Finite difference method for calculating steady incompressible flows in 3-D', *J. Comput. Phys.*, **33**, 325–339 (1979).
32. J. B. Cazalbou, M. Braza and H. Ha Minh, 'A numerical method for computing three-dimensional Navier–Stokes equations applied to cubic cavity flows with heat transfer', in *Numerical Methods in Laminar and Turbulent Flows*, Vol. 4, Pineridge, Swansea, 1983, pp. 786–797.
33. J. R. Koseff, R. L. Street, P. M. Gresho, C. D. Upson, J. A. C. Humphrey and W. M. To, 'A three-dimensional lid-driven cavity flow: experiment and simulation', in *Numerical Methods in Laminar and Turbulent Flows*, Vol. 4, Pineridge, Swansea, 1983, pp. 564–581.
34. J. Kim and P. Moin, 'Application of a fractional-step method to incompressible Navier–Stokes equations', *J. Comput. Phys.*, **59**, 308–323 (1985).
35. S. P. Vanka, 'A calculation procedure for three-dimensional recirculating flows,' *Comput. Methods Appl. Mech. Eng.*, **55**, 321–328 (1986).
36. G. A. Osswald, U. Ghia and K. N. Ghia, 'A direct algorithm for solution of incompressible three-dimensional unsteady Navier–Stokes equations', *AIAA Paper 87-1139*, 1987.
37. C. Y. Perng and R. L. Street, 'Three-dimensional unsteady flow simulations: alternative strategies for a volume-averaged calculation', *Int. j. numer methods fluids*, **9**, 341–362 (1989).
38. D. P. Hwang and H. T. Huynh, 'A finite difference scheme for three-dimensional steady laminar incompressible flow', in *Numerical Methods in Laminar and Turbulent Flows*, Vol. 5, Pineridge, Swansea, 1987, pp. 244–260.
39. A. Orth and B. Schönung, 'Calculation of 3-D laminar flows with complex boundaries using a multigrid method', in P. Wesseling (ed.), *Notes on Numerical Fluid Mechanics*, Vol. 23, Vieweg, Braunschweig, 1990, pp. 446–453.
40. H. Kawai, Y. Kato, T. Sawada and T. Tanahashi, 'GSMAC-FEM for incompressible viscous flow analysis (a modified GSMAC method)', *JSME Int. J.*, **33**, 17–30 (1990).
41. H. C. Ku, R. S. Hirsh and T. D. Taylor, 'A pseudospectral method for the solution of the three dimensional incompressible Navier–Stokes equations', *J. Comput. Phys.*, **70**, 439–462 (1987).
42. C. F. Freitas, R. L. Street, A. N. Finditakis and J. R. Koseff, 'Numerical simulation of three-dimensional flow in a cavity', *Int. j. numer. methods fluids*, **5**, 561–575 (1985).
43. R. Iwatsu, K. Ishii, T. Kawamura, K. Kuwahara and J. M. Hyun, 'Numerical simulation of three-dimensional flow structure in a driven cavity', *Fluid Dyn. Res.*, **5**, 173–189 (1989).
44. J. R. Koseff and R. L. Street, 'Visualization studies of a shear driven three-dimensional recirculation flow', *J. Fluids Eng.*, **106**, 21–29 (1984).
45. J. R. Koseff and R. L. Street, 'On end-wall effects in a lid-driven cavity flow', *J. Fluids Eng.*, **106**, 385–389 (1984).
46. J. R. Koseff and R. L. Street, 'The lid-driven cavity flow: a synthesis of qualitative and quantitative observations', *J. Fluids Eng.*, **106**, 390–398 (1984).